TECHNICAL REVIEW

Beamforming

No.1 2004

Brüel & Kjær

Previously issued numbers of
Brüel & Kjær Technical Review

Technical Review

No. 1 – 2004

Contents

Beamforming

by J.J. Christensen and J. Hald

Abstract

This article explains the basic principles of Beamforming, including the main performance parameters Resolution and Sidelobe Level. Special attention is given to the influence of array design and to cross-spectral beamforming. Different array designs, including Brüel & Kjær's newly patented wheel array design, are described and compared, and the basic principle of Brüel & Kjær's geometry optimisation method is outlined. A new, improved version of cross-spectral beamforming used in Beamforming Software Type 7768 is introduced and its benefits are verified. The article also provides some guidelines for performing good measurements and finally, describes a set of measurements representing typical applications.

Résumé

Cet article traite succintement du concept d'imagerie par formation de faisceaux, et notamment des principaux paramètres essentiels aux performances de l'antenne que sont la Résolution et le Niveau de lobe latéral. Une attention toute particulière est portée sur l'influence de la forme de l'antenne et sur la formation de faisceaux par approche interspectrale. Diverses conceptions d'antennes, dont l'antenne circulaire Brüel & Kjær nouvellement brevetée, y sont présentées et comparées; les principes fondamentaux de la méthode propriétaire d'optimisation géométrique y sont soulignés. Une nouvelle version amendée de l'approche interspectrale implémentée dans le Logiciel Beamforming Software Type 7768 est également présentée et ses avantages sont vérifiés. Cet article inventorie par ailleurs les points contribuant à la réalisation de mesures de qualité, pour conclure par la description d'une série de mesures se rapportant à des applications typiques.

Zusammenfassung

Dieser Artikel erläutert die Grundprinzipien des Beamforming einschließlich der Hauptparameter Auflösung und Nebenmaxima (Sidelobe Level). Besondere Aufmerksamkeit wird dem Einfluss der Array-Konstruktion und dem Beamforming nach dem Kreuzspektrum-Verfahren gewidmet. Es werden verschiedene Array-

Konstruktionen beschrieben und verglichen, darunter Brüel & Kjærs patentiertes Wheel Array. Außerdem wird das Grundprinzip der Geometrieoptimierung von Brüel & Kjær skizziert. Eine neue verbesserte Version des in der Beamforming Software Typ 7768 verwendeten Beamforming nach dem Kreuzspektrum-Verfahren wird vorgestellt und dessen Vorteile nachgewiesen. Der Artikel enthält auch Richtlinien zur Durchführung guter Messungen und beschreibt eine Serie von Messungen, die typische Anwendungen repräsentieren.

Introduction

Planar Near-field Acoustical Holography (NAH) is an established technique for efficient and accurate noise source location [1, 2]. NAH can provide high-resolution source maps on a planar source surface from measurements taken over a regular rectangular grid of points close to the source. The measurement grid must capture the major part of the sound radiation into a half space and therefore completely cover the noise source plus approximately a 45° solid angle. The grid spacing must be less than half a wavelength at the highest frequency of interest. Thus, the number of measurement points gets very high when the source is much larger than the wavelength, which always occurs at sufficiently high frequencies. The same problem arises when for some reason it is not possible to measure close to the source. Then, because of the required 45° coverage angle, the measurement area must be very large. In these cases, beamforming is an attractive alternative.

Beamforming is an array-based measurement technique for sound-source location from medium to long measurement distances. Basically, the source location is performed by estimating the amplitudes of plane (or spherical) waves incident towards the array from a chosen set of directions. The angular resolution is inversely proportional to the array diameter measured in units of wavelength, so the array should be much larger than wavelength to get a fine angular resolution. At low frequencies, this requirement usually cannot be met, so here the resolution will be poor. Unlike NAH, beamforming does not require the array to be larger than the sound source. For typical, irregular array designs, the beamforming method does not allow the measurement distance to be much smaller than the array diameter. On the other hand, the measurement distance should be kept as small as possible to achieve the finest possible resolution on the source surface.

An important difference between beamforming and NAH is that beamforming can use irregular array geometries, for example, random array geometries. The use of a discrete set of measurement points on a plane can be seen as a spatial sampling

of the sound field. NAH requires a regular, rectangular grid of points in order to apply a 2D spatial DFT. Outside the near-field region, such a regular grid will suppress spatial aliasing effects very well, if the grid spacing is just less than half a wavelength. When the grid spacing exceeds half a wavelength, spatial aliasing components quickly get very disturbing. Irregular arrays on the other hand can potentially provide a much smoother transition: spatial aliasing effects can be kept at an acceptable level up to a much higher frequency with the same average spatial sampling density. This indicates why beamforming can measure up to high frequencies with a fairly low number of microphones.

Theory

Delay-And-Sum Beamforming for Infinite Focus Distance
The principle of Beamforming is best introduced through a description of the basic Delay-and-Sum beamformer. As illustrated in Fig. 1, we consider a planar array of M microphones at locations $\mathbf{r}_m$ ($m = 1, 2, …, M$) in the xy-plane of our coordinate system. When such an array is applied for Delay-and-Sum Beamforming, the measured pressure signals p_m are individually delayed and then summed [3]:

Fig. 1. (a) A microphone array, a far-field focus direction, and a plane wave incident from the focus direction. (b) A typical directional sensitivity diagram with a main lobe in the focus direction and lower sidelobes in other directions

3
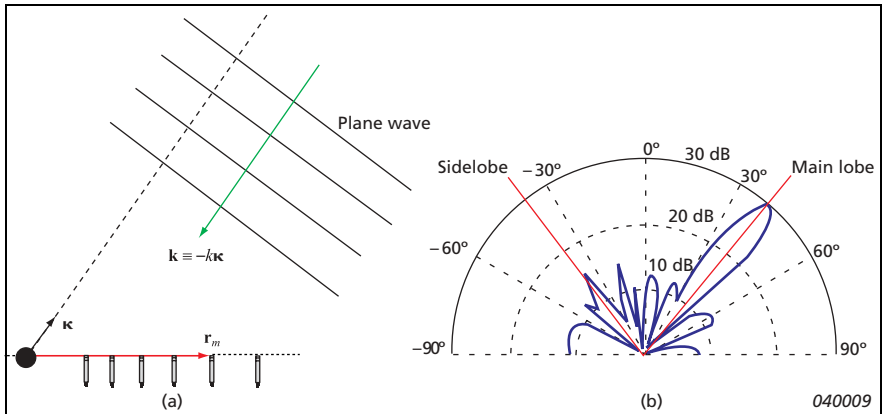
$$b(\boldsymbol{\kappa}, t) = \sum_{m=1}^{M} w_m p_m(t - \Delta_m(\boldsymbol{\kappa})) \tag{1}$$

where w_m are a set of weighting or *shading* coefficients applied to the individual microphone signals. The individual time delays Δ_m are chosen with the aim of achieving selective directional sensitivity in a specific direction, characterised here by a unit vector $\boldsymbol{\kappa}$. This objective is met by adjusting the time delays in such a way that signals associated with a plane wave, incident from the direction $\boldsymbol{\kappa}$, will be aligned in time before they are summed. Geometrical considerations (Fig. 1) show that this can be obtained by choosing:

$$\Delta_m = \frac{\boldsymbol{\kappa} \cdot \mathbf{r}_m}{c} \tag{2}$$

where c is the propagation speed of sound. Signals arriving from other far-field directions will not be aligned before the summation, and therefore they will not add up coherently. Thus, we have obtained a directional sensitivity, as illustrated in Fig. 1(b).

The frequency domain version of eq. (1) for the Delay-and-Sum beamformer output is:

$$B(\boldsymbol{\kappa}, \omega) = \sum_{m=1}^{M} w_m P_m(\omega) e^{-j\omega \Delta_m(\boldsymbol{\kappa})} = \sum_{m=1}^{M} w_m P_m(\omega) e^{j\mathbf{k} \cdot \mathbf{r}_m} \tag{3}$$

Here, ω is the temporal angular frequency, $\mathbf{k} \equiv -k\boldsymbol{\kappa}$ is the wave number vector of a plane wave incident from the direction $\boldsymbol{\kappa}$ in which the array is focused (see Fig. 1), and $k = \omega/c$ is the wave number. In eq. (3) an implicit time factor equal to $e^{j\omega t}$ is assumed. Because $\mathbf{k} \equiv -k\boldsymbol{\kappa}$, we can write $B(\mathbf{k}, \omega)$ instead of $B(\boldsymbol{\kappa}, \omega)$.

Through our choice of time delays $\Delta_m(\boldsymbol{\kappa})$, or equivalently of the "preferred" wave number vector $\mathbf{k} \equiv -k\boldsymbol{\kappa}$, we have "tuned" the beamformer on the far-field direction $\boldsymbol{\kappa}$. Ideally, we would like to measure only signals arriving from that direction, in order to get a perfect localisation of the sound sources. To investigate, how much "leakage" we will get from plane waves incident from other directions, we now assume a plane wave incident with a wave number vector $\mathbf{k}_0$ different from the preferred $\mathbf{k} \equiv -k\boldsymbol{\kappa}$, Fig. 2. The pressure measured by the microphones will then be:

$$P_m(\omega) = P_0 e^{-j\mathbf{k}_0 \cdot \mathbf{r}_m} \tag{4}$$

which, according to eq. (3), will give the following output from the beamformer:

Fig. 2. A plane wave, with wave number vector $\mathbf{k}_0$, incident from a direction different from the focus direction $\mathbf{\kappa}$. For a planar array the beamformer output, eq. (5), is a function of the difference $\mathbf{K}$ of the projections $\hat{\mathbf{k}}_0$ and $\hat{\mathbf{k}}$ of the wave number vectors $\mathbf{k}_0$ and $\mathbf{k}$ onto the plane defined by the array
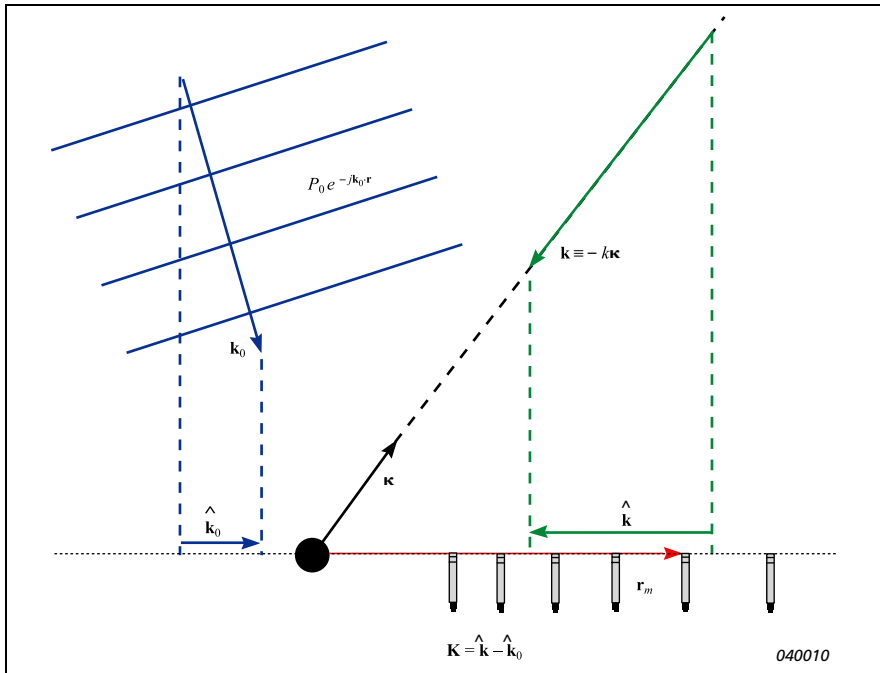
$$B(\mathbf{\kappa}, \omega) \;=\; P_0 \sum_{m=1}^{M} w_m e^{j(\mathbf{k} - \mathbf{k}_0) \cdot \mathbf{r}_m} \equiv P_0 W(\mathbf{k} - \mathbf{k}_0) \tag{5}$$

Here, the function W,

$$W(\mathbf{K}) \equiv \sum_{m=1}^{M} w_m e^{j\mathbf{K} \cdot \mathbf{r}_m} \tag{6}$$

is the so-called *Array Pattern*. It has the form of a generalised spatial DFT of the weighting function w, which equals zero outside the array area. In the case of *uniform shading*, $w_m \equiv 1$, the array pattern, eq. (6), depends only on the array geometry. In the following we shall mainly be concerned with uniform shading and will

5

consequently omit the w_m term from the equations. The effect of non-uniform shading is discussed in "Regular Arrays" on page 19.

Because the microphone positions $\mathbf{r}_m$ have z-coordinate equal to zero, the Array Pattern, eq. (6), is independent of K_z. We shall therefore consider the Array Pattern W only in the (K_x, K_y) plane, that is, we consider the projections of the wave number vectors onto that plane, Fig. 2. There, W has an area with high values around the origin, with a peak value equal to M at $(K_x, K_y) = (0, 0)$. According to eq. (5), this peak represents the high sensitivity to plane waves coming from the direction $\boldsymbol{\kappa}$, in which the array is focused. Fig. 1 contains an illustration of that peak, which is called the *main lobe*. Other directional peaks are called *sidelobes*. Fig. 1 contains information about only a single frequency and a single focus direction. Eq. (5) shows that the array pattern, eq. (6), contains information about the sidelobe structure for all focus directions and all frequencies. Fig. 3 depicts a section of the array pattern corresponding to the array geometry depicted in Fig. 4.

Fig. 3. Contour plot of the Array Pattern, eq. (6), corresponding to the array depicted in Fig. 4. For a given upper frequency, $\omega_{\max}$, of the array's intended use, all sidelobes between the main lobe radius $K_{\min}^0$ and the circle $K_{\max}^{90°} = 2\omega_{\max}/c$ must be taken into account. When beamformer focusing is restricted to be within 30° of the array axis, only sidelobes for wave numbers below $K_{\max}^{30°} = (3/2)\omega_{\max}/c$ are relevant

040011
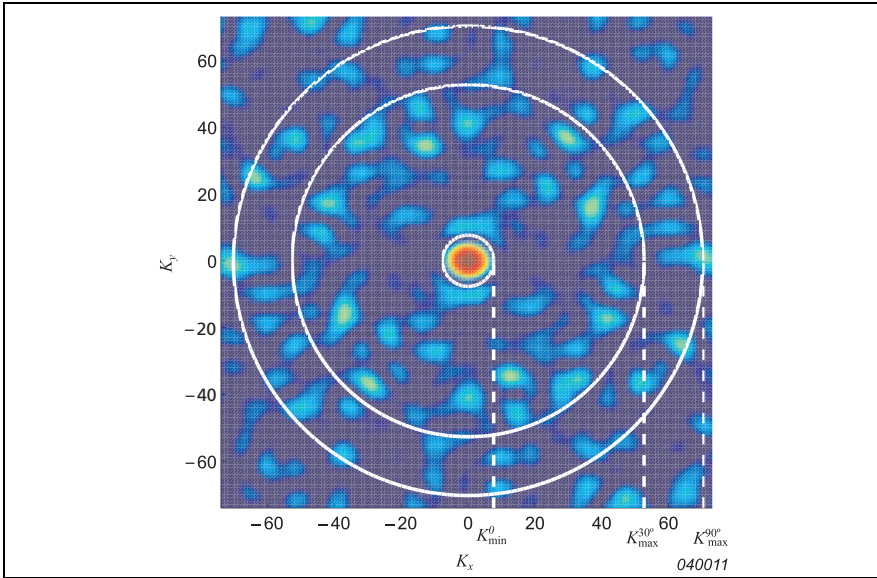
Fig. 4. An example of a planar 66-channel beamformer array and its equivalent circular aperture (---). The microphone positions (●) are randomly distributed over the circular aperture

040012
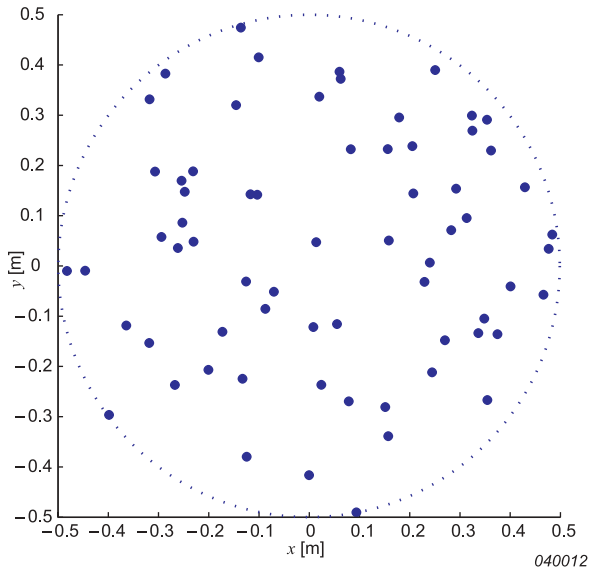
A sidelobe (a peak in the array pattern different from the peak at the origin) will, according to eq. (5), have the effect that a single incident plane wave will be measured with a significant level when focusing in a specific direction not equal to the direction from which the plane wave is actually incident. The sidelobes will therefore create so-called *Ghost Images* in measured directional source maps. The level of the sidelobes relative to the main lobe (the dynamic range) defines the ability of the beamformer to suppress ghost images.

Normalisation

In the case of perfect focus, $\mathbf{k} = \mathbf{k}_0$, the delay-and-sum beamformer, eq. (5), amplifies the input signal by the number of channels: $B(-\mathbf{k}_0/k, \omega) = MP_0$. For this reason the delay-and-sum beamformer is often normalised by the number of channels:

$$B(\boldsymbol{\kappa}, \omega) = \frac{1}{M} \sum_{m=1}^{M} P_m(\omega) e^{j\mathbf{k} \cdot \mathbf{r}_m} \tag{7}$$

7

Resolution

The resolution of a beamformer describes its ability to distinguish waves incident from directions close to each other. When focusing on sources in the far field, resolution is the smallest angular separation between two plane waves that allows them to be separated, and for sources at a finite distance a practical definition of resolution is the minimum distance between two sources such that they can be separated.

Consider two plane waves with wave number vectors $\mathbf{k}_1$ and $\mathbf{k}_2$, $|\mathbf{k}_1| = |\mathbf{k}_2| = k$, incident on a beamformer array with array pattern W. Assuming unity amplitude for both plane waves, the beamformer output is a superposition of the form:

Fig. 5. The curves show the beamformer output, $B(\kappa, \omega)$, cf. eq. (8) resulting from two plane waves with wave number vectors $\mathbf{k}_1$ and $\mathbf{k}_2$ incident on a planar array. The Rayleigh criterion for resolution states that the two directions can be resolved when the peak of the shifted array pattern $W(\mathbf{k} - \mathbf{k}_2)$ corresponding to the plane wave with angle of incidence, θ, falls on the first zero (or minimum) of $W(\mathbf{k} - \mathbf{k}_1)$

8
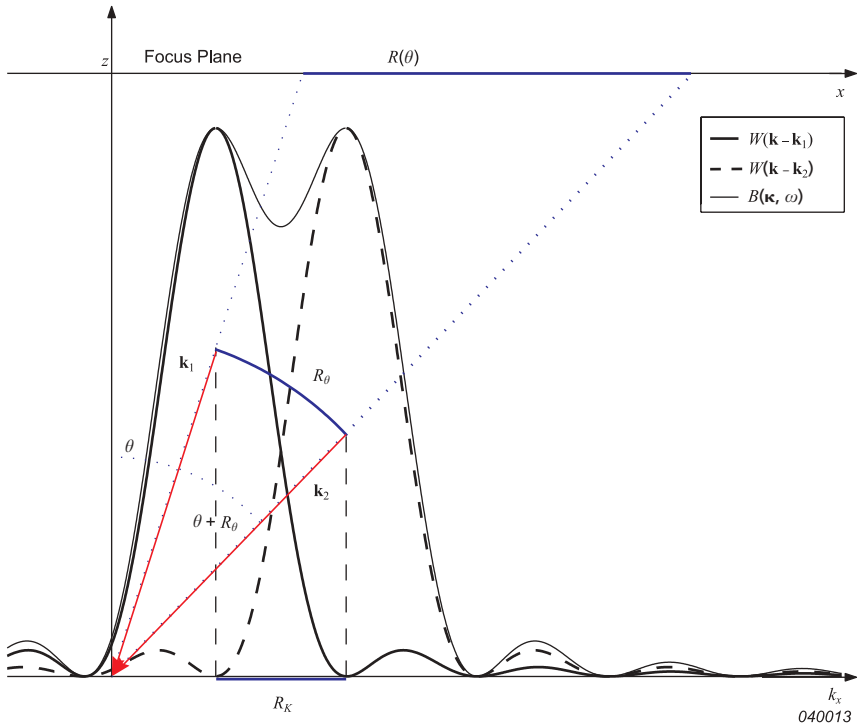
$$B(\boldsymbol{\kappa}, \omega) = W(\mathbf{k} - \mathbf{k}_1) + W(\mathbf{k} - \mathbf{k}_2) \tag{8}$$

cf. eq. (5). The *Rayleigh criterion* [3] states that the two directions can be just exactly resolved when the peak of $W(\mathbf{k} - \mathbf{k}_2)$ falls on the first zero of $W(\mathbf{k} - \mathbf{k}_1)$, cf. Fig. 5. Assuming that the required angular separation between $\mathbf{k}_1$ and $\mathbf{k}_2$ is small, it can be shown (see "Appendix: Resolution" on page 47) that at finite distance, z, the minimum resolvable source separation in the radial direction, $R(\theta)$, is given by:

$$R(\theta) = \frac{zR_K}{k}\frac{1}{\cos^3\theta} \tag{9}$$

where R_K is the main lobe width in the array pattern and θ is the off-axis angle. The value of R_K is, according to the Rayleigh criterion, given by the first null (minimum), $K_{\min}^0$, of the array pattern: $R_K = K_{\min}^0$. The exact value depends on the positions of all the array microphones through eq. (6), but a good general estimate can be calculated by considering the limiting cases where we have an infinite number of transducers uniformly distributed over a line segment of length D or a circular disc with radius $D/2$. In other words, we imagine we are able to sample the sound field at all points within an area (aperture) instead of only at a few discrete positions. In this continuous case we should use an integral expression for the array pattern, eq. (6), the *aperture smoothing function*:

$$W(\mathbf{K}) = \frac{1}{(2\pi)^d}\int_{|\mathbf{r}| < D/2} w(\mathbf{r})e^{j\mathbf{K}\cdot\mathbf{r}}d^d\mathbf{r} \tag{10}$$

where $d = 1$ for the line segment, $d = 2$ for the circular aperture and $w(\mathbf{r})$ is now a continuous shading function. In the case of uniform shading, eq. (10) can be evaluated to, J_1 being the Bessel function of order 1 [3]:

$$W(K_x) = \frac{\sin(K_x D/2)}{K_x/2}, \qquad d = 1 \tag{11}$$

$$W(K) = \frac{\pi D}{K}J_1(KD/2), \qquad K = \sqrt{K_x^2 + K_y^2}, \qquad d = 2 \tag{12}$$

From eq. (11) and eq. (12) we find that the first zero in the array pattern corresponding to the line segment and the circular aperture occurs at:

$$K_{\min}^0 = a\frac{2\pi}{D} \tag{13}$$

where $a = 1$ for the linear aperture and $a \approx 1.22$ for the circular aperture. Now, using the fact that the wave number k is related to the wavelength, λ, by $k = 2\pi/\lambda$ we obtain by insertion into eq. (9) the desired expression for beamformer resolution:

$$R(\theta) = \frac{a}{\cos^3\theta} \frac{z}{D} \lambda \tag{14}$$

For on-axis incidence, $\theta = 0$, the resolution is given by:

$$R_{\text{Axis}} = a\left(\frac{z}{D}\right)\lambda \tag{15}$$

We notice that the resolution is proportional to the wavelength and becomes better with larger aperture size, but worse with increasing array to object distance. This relation is not limited to acoustics; the reader may be familiar with the fact that the ability of an optical camera to resolve details depends on the lens diameter and the distance to the object.

Comparing the on-axis and general off-axis resolution, eq. (15) and eq. (14), we notice that the ratio between them is given by:

$$\frac{R(\theta)}{R_{\text{Axis}}} = \frac{1}{\cos^3\theta} \tag{16}$$

This ratio is depicted in Fig. 6 and we observe that for angles of incidence more than 30° off-axis, the resolution becomes more than 50% greater than the on-axis resolution. For this reason the useful beamformer opening angle is in practice restricted to 30°.

Fig. 6. The variation of the ratio between off-axis and on-axis resolution as given by eq. (16)

040014
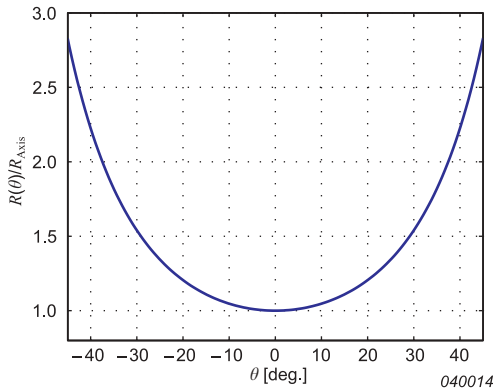
Maximum Sidelobe Levels

The presence of sidelobes in the directivity pattern (Fig. 1) or, correspondingly, in the array pattern, will cause waves from non-focus directions to leak into the measurement of the main lobe direction $\boldsymbol{\kappa}$. This will produce false peaks/sources in a measured directional source map. A good phased array design can therefore be characterised by having low *Maximum Sidelobe Level* (*MSL*), measured relative to the main lobe level. We define the radial profile of the array pattern, $W_p(K)$, by:

$$W_p(K) \equiv 10 \cdot \log_{10}\left[\max_{|\mathbf{K}|\,=\,K} |W(\mathbf{K})|^2 / M^2\right] \tag{17}$$

and based on this profile we define the Maximum Sidelobe Level function as:

$$MSL(K) \equiv \max_{K_{\min}^0 < K' \le K} W_p(K') = 10 \cdot \log_{10}\left[\max_{K_{\min}^0 < |\mathbf{K}| \le K} |W(\mathbf{K})|^2 / M^2\right] \tag{18}$$

where $K_{\min}^0$ is given by eq. (13). A comparison of the radial profile, W_p, for a particular discrete array and its corresponding circular aperture is given in Fig. 7. The *MSL* function for the same discrete array is shown in Fig. 8.

For practical use of the array pattern, its radial profile and the *MSL* function, it is important to know which part of the array pattern is "active", when the array is used at a specific frequency. With reference to eq. (5), the argument to the array pattern is the difference vector $\mathbf{k}(\boldsymbol{\kappa}) - \mathbf{k}_0$ between the wave number vector $\mathbf{k}$ of the in-focus plane wave and the wave number vector $\mathbf{k}_0$ of the incident plane wave. Both $\mathbf{k}$ and $\mathbf{k}_0$ have length equal to the wave number k, and the difference vector has maximum length when the two plane waves have opposite directions – pointing, for example, in the positive and negative x-axis directions – meaning that $|\mathbf{k} - \mathbf{k}_0| \le 2k$ (see Fig. 2). Therefore, at a given frequency ω, only the section $|\mathbf{K}| \le 2k = 2\omega/c$ of the Array Pattern will be "visible". If we restrict the focus direction $\boldsymbol{\kappa}$ to be within an angle θ from the array axis, then the maximum length of the difference vector reduces, so only the section $|\mathbf{K}| \le K_{\max}^\theta(\omega)$ of the array pattern will be visible with:

$$K_{\max}^\theta(\omega) \equiv [1 + \sin(\theta)]\frac{\omega}{c} \tag{19}$$

If the Array Pattern has low *MSL* for $|\mathbf{K}| \le K_{\max}$, then a beamformer application will provide accurate directional source maps with a low degree of false images up to the frequency $\omega_{\max}$ given by (Fig. 3):

Fig. 7. Comparison of the aperture smoothing function, eq. (12), for a circular aperture and the radial array pattern profile of eq. (18) for a "circular" 66-channel discrete array with the same diameter (Fig. 4). The aperture smoothing function of the uniformly shaded circular aperture represents the, theoretically, best sidelobe suppression attainable. Due to the finite number of points sampled with the discrete array, the sidelobe levels are much higher. The main lobe widths of the discrete array and the equivalent circular aperture are nearly identical as this quantity is determined by the aperture size
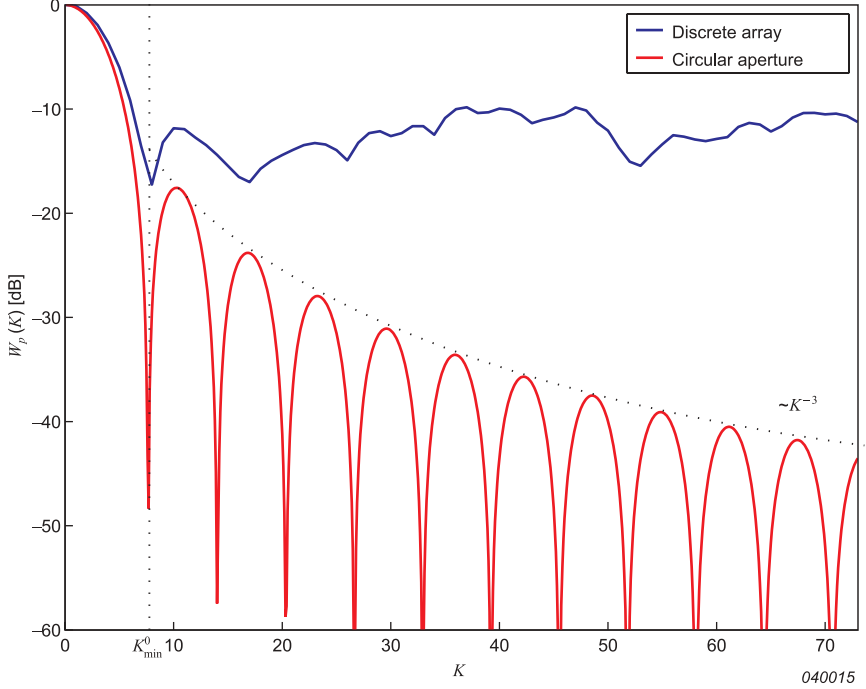
$$K^\theta_{\max}(\omega_{\max}) = K_{\max} \quad \Rightarrow \quad \omega_{\max}(\theta) = \frac{K_{\max}c}{1 + \sin(\theta)} \tag{20}$$

As an example, if the beamformer will be focused on directions $\boldsymbol{\kappa}$ not more than 30° off-axis, then the upper limiting frequency becomes $\omega_{\max}(30°) = {}^2\!/_3 K_{\max}c$ (Fig. 3). We notice the general relation:

$$\omega_{\max}(30°) = \frac{4}{3}\omega_{\max}(90°) \tag{21}$$

12

Fig. 8. The sidelobe level profile, W_p, eq. (17) and the maximum sidelobe level function
MSL(K), eq. (18), for the array depicted in Fig. 4. The functions are extracted from the corre-
sponding array pattern of Fig. 3
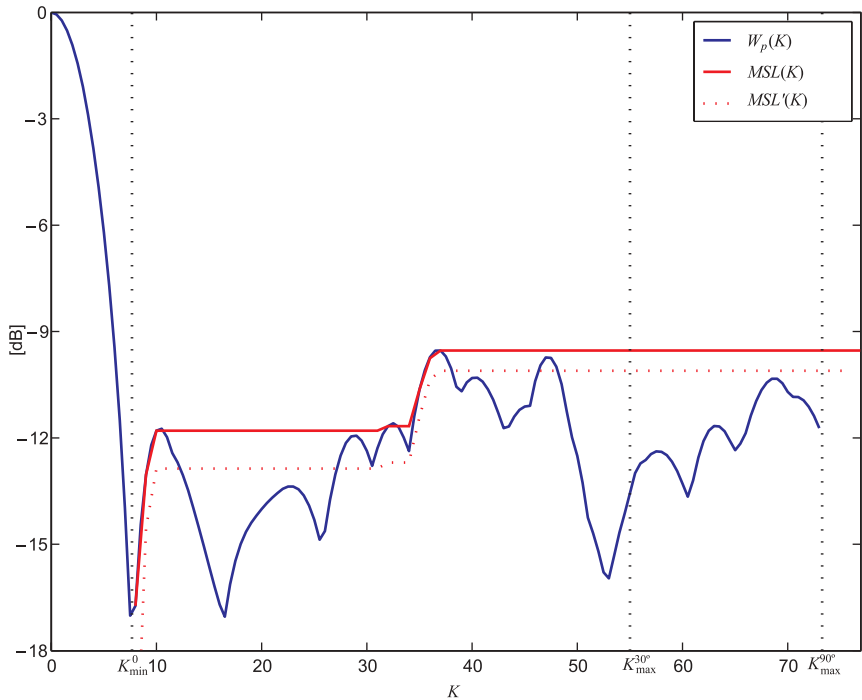
040016

Eq. (19) is a linear relation between frequency ω and the highest array pattern
wave number $K = K_{\max}^{\theta}(\omega)$ that is active at that frequency. The argument K of
the *MSL* function, eq. (18), is exactly an upper limiting wave number in the array
pattern, so therefore it is straightforward to use $K = K_{\max}^{\theta}(\omega)$ as argument in the
MSL function. Thereby we have expressed the *MSL* as a function of frequency ω:
$MSL[K_{\max}^{\theta}(\omega)]$. In order to calculate the *MSL* at a given frequency, one needs to
specify the maximum focusing angle θ. We have chosen to always show or specify
the worst case $MSL[K_{\max}^{90°}(\omega)]$, that is, no restriction on focus direction.

Cross-spectral Formulation with Exclusion of Autospectra

For stationary sound fields it is natural to operate with averaged cross- and auto-
spectra, and it turns out that exclusion of autospectra in beamforming calculations

13

is advantageous in several respects. The average power output from the Delay-and-Sum beamformer can be derived from eq. (3):

$$V(\boldsymbol{\kappa}, \omega) \equiv \overline{|B(\boldsymbol{\kappa}, \omega)|^2} = \sum_{m, n = 1}^{M} \overline{P_m(\omega)P_n{}^*(\omega)} e^{j\mathbf{k} \cdot (\mathbf{r}_m - \mathbf{r}_n)}$$

$$= \sum_{m, n = 1}^{M} C_{nm}(\omega) e^{j\mathbf{k} \cdot (\mathbf{r}_m - \mathbf{r}_n)} \qquad (\text{* indicates complex conjugate}) \qquad (22)$$

where we have introduced the cross-spectrum matrix:

$$C_{nm}(\omega) \equiv \overline{P_m(\omega)P_n{}^*(\omega)}$$

We may split eq. (22) into an autospectrum part and a cross-spectrum part:

$$V(\boldsymbol{\kappa}, \omega) = \sum_{m = 1}^{M} C_{mm} + \sum_{m \neq n}^{M} C_{nm} e^{j\mathbf{k} \cdot (\mathbf{r}_m - \mathbf{r}_n)} \qquad (23)$$

Here, the autospectra C_{mm} will contain self-noise from the individual channels, such as wind-noise and electronic noise from the data acquisition hardware. For that reason it would be desirable to omit the first sum in eq. (23). Ideally, the cross-spectra C_{nm}, $m \neq n$, are not affected by the self-noise, because the self-noise in one channel is generally incoherent with the self-noise in any other channel. Under that condition, averaging will suppress contributions from self-noise in the cross-spectra. We can assess the effect of excluding the autospectra by considering the plane wave response of the cross-spectral beamformer. For a plane wave with wave number vector $\mathbf{k}_0$ and amplitude P_0 the pressure recorded by the mth micro-phone is $P_m = P_0\exp(-j\mathbf{k}_0\mathbf{r}_m)$. Insertion of this in eq. (22) leads to the following expression for the beamformer power output:

$$V(\boldsymbol{\kappa}, \omega) = |P_0|^2 \sum_{m, n = 1}^{M} e^{-j\mathbf{k}_0 \cdot (\mathbf{r}_m - \mathbf{r}_n)} e^{j\mathbf{k} \cdot (\mathbf{r}_m - \mathbf{r}_n)}$$

$$= |P_0|^2 \sum_{m, n = 1}^{M} e^{j(\mathbf{k} - \mathbf{k}_0) \cdot (\mathbf{r}_m - \mathbf{r}_n)} = |P_0|^2 U(\mathbf{k} - \mathbf{k}_0) \qquad (24)$$

where we have introduced the *Power Array Pattern*:

14

$$U(\mathbf{K}) \equiv |W(\mathbf{K})|^2 = \sum_{m,n=1}^{M} e^{j\mathbf{K}\cdot(\mathbf{r}_m-\mathbf{r}_n)} \tag{25}$$

In a similar way we see that the self-term-free versions of the power array pattern, eq. (25), and the cross-spectral beamformer response, eq. (23):

$$U'(\mathbf{K}) \equiv \sum_{m \neq n}^{M} e^{j\mathbf{K}\cdot(\mathbf{r}_m-\mathbf{r}_n)} \quad \text{and} \quad V'(\boldsymbol{\kappa},\omega) \equiv \sum_{m \neq n}^{M} C_{nm} e^{j\mathbf{k}\cdot(\mathbf{r}_m-\mathbf{r}_n)} \tag{26}$$

are for plane waves related by:

$$V'(\boldsymbol{\kappa},\omega) = |P_0|^2 U'(\mathbf{k}-\mathbf{k}_0) \tag{27}$$

Thus, removal of the autospectral terms from the cross-spectral beamformer, eq. (23), corresponds to omitting the self-terms from the definition of the power array pattern, eq. (25). Provided the reduced array pattern U' has lower sidelobe level than U, we can therefore reduce the level of ghost images in cross-spectral beamformer output by omitting the autospectra.

Comparing the definitions of the array pattern U and the reduced version U' we find that:

$$U'(\mathbf{K}) = U(\mathbf{K}) - M \tag{28}$$

The main lobe is therefore reduced from M^2 (for U) to $M^2 - M$ (for U'), and the highest sidelobe is reduced from $M^2 \cdot 10^{MSL/10}$ to $M^2 \cdot 10^{MSL/10} - M$. Assuming first that U' does not become negative, this leads to the following Maximum Sidelobe Level for U':

$$MSL' = 10 \cdot \log_{10}\left(\frac{M^2 \cdot 10^{MSL/10} - M}{M^2 - M}\right) = 10 \cdot \log_{10}\left(\frac{M \cdot 10^{MSL/10} - 1}{M - 1}\right)$$

which is easily shown to be always smaller (better) than MSL. As an example, for the 66-channel array depicted in Fig. 4, the MSL equals -9.5 dB over a wide frequency range. Over that frequency range MSL' equals -10.1 dB, meaning that the highest sidelobe has been reduced by 0.6 dB (Fig. 8). At lower frequencies the gain is bigger. If the power array pattern U contains values less than M, then the reduced array pattern U' will have areas with negative values. The worst case is when U has a null. In that case the minimum value of U' equals $-M$, which will have the same effect as a sidelobe with amplitude equal to M. Such a sidelobe will not affect MSL' as long as M is smaller than $M^2 \cdot 10^{MSL/10} - M$. This condition has

been fulfilled for all the arrays that we have been designing. Additionally, this worst-case condition will not occur, when only array geometries without redundant spacing vectors are used.

Finite Focus Distance

Up to now we have only considered the resolution of incoming plane waves, corresponding to point sources at infinite distance. The time delays Δ_m of eq. (2) were chosen with the aim of aligning in time the signals of a plane wave arriving from the far-field direction $\boldsymbol{\kappa}$ before the summation of the Delay-And-Sum beamforming, eq. (1). Use of a plane wave for calculation of the delays corresponds to focusing of the array at infinite distance in the chosen direction. To focus on a point source at a finite distance, the delays should align in time the signals of a spherical wave radiated from the focus point.

The expression for Delay-And-Sum beamforming for focusing at a point $\mathbf{r}$ at a finite distance becomes:

$$B(\mathbf{r}, \omega) = \sum_{m=1}^{M} P_m(\omega) e^{-j\omega \Delta_m(\mathbf{r})} \tag{29}$$

Here we have replaced the delays, eq. (2), with the form:

$$\Delta_m(\mathbf{r}) = \frac{|\mathbf{r}| - r_m(\mathbf{r})}{c} \tag{30}$$

where $r_m(\mathbf{r}) \equiv |\mathbf{r} - \mathbf{r}_m|$ is the distance from microphone m to the focus point, Fig. 9. The near-field version of eq. (23) for the beamformer power output appears as:

$$V(\mathbf{r}, \omega) = \sum_{m=1}^{M} C_{mm} + \sum_{m \neq n}^{M} C_{nm} e^{j\omega[\Delta_n(\mathbf{r}) - \Delta_m(\mathbf{r})]} \tag{31}$$

Cross-spectral Imaging Function

Eq. (31) for finite-distance beamforming contains no compensation for the fact that different positions on the assumed source plane have different distances to the array transducers and therefore are attenuated by different amounts. For a single source at $\mathbf{r}_i$, a possible correction could be to replace the cross-spectrum matrix by the scaled version $C_{nm} r_m(\mathbf{r}_i) r_n(\mathbf{r}_i)$. The introduction of a scaled cross-spectrum matrix is, however, an ad-hoc correction with uncontrolled effects. A sound approach can be achieved by assuming a model where the recorded sound field is generated by a monopole distribution. For each position on the source plane the

16

Fig. 9. In near-field focusing, spherical waves emitted by a monopole source at the focus point $\mathbf{r}$ are assumed. Signal delays are computed according to eq. (30)
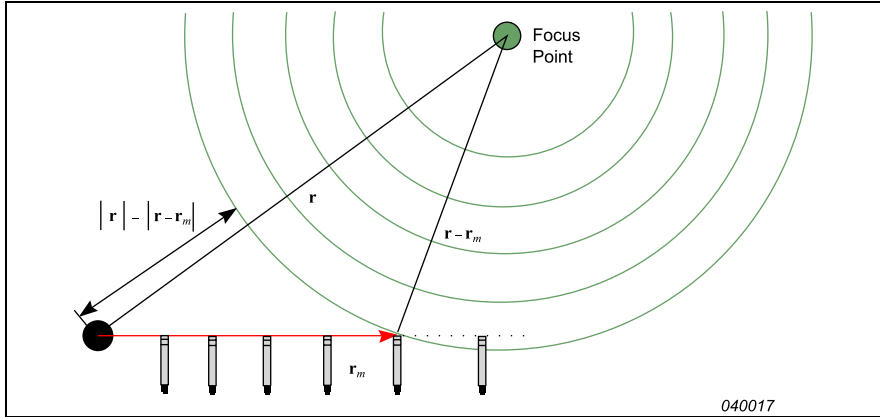
estimated source strength reflects how well the sound field from a monopole point source at that position fits the sound field measured by the array.

Let $\mathbf{r}_m$, $m = 1, \ldots, M$, be the transducer coordinates and let $\mathbf{r}$ be the position of a monopole. The pressure, P_m, recorded by the mth transducer is then given by $P_m(\mathbf{r}) \equiv P_0 v_m(\mathbf{r}) = P_0 v(\mathbf{r}_m - \mathbf{r})$, where P_0 is the source strength and $v(\mathbf{r})$ is the steering vector given by:

$$v(\mathbf{r}) = e^{-jk|\mathbf{r}|}/|\mathbf{r}| \tag{32}$$

and the cross-spectrum, C_{nm}^{mod}, between channel m and n is:

$$C_{nm}^{\text{mod}} = P_n^* P_m = a v_n^*(\mathbf{r}) v_m(\mathbf{r}) \tag{33}$$

where a is a real amplitude coefficient. Then we define an error function, $E(a, \mathbf{r})$, between the model cross-spectra and the measured cross-spectra, C_{nm}:

$$E(a, \mathbf{r}) = \sum_{m, n = 1}^{M} \left| C_{nm} - C_{nm}^{\text{mod}} \right|^2 = \sum_{m, n = 1}^{M} \left| C_{nm} - a v_n^*(\mathbf{r}) v_m(\mathbf{r}) \right|^2 \tag{34}$$

As shown in "Appendix: The Cross-spectral Imaging Function" on page 43, the minimisation of this error function corresponds to the maximisation of the *Cross-spectral Imaging Function* defined by:

17

$$I^2(\omega, \mathbf{r}) \equiv \frac{1}{M} \frac{\left| \sum_{m, n = 1}^{M} C_{nm}(\omega) v_n(\mathbf{r}) v_m^*(\mathbf{r}) \right|}{\sqrt{\sum_{m, n = 1}^{M} |v_n(\mathbf{r})|^2 |v_m(\mathbf{r})|^2}} \tag{35}$$

In practice $I^2(\omega, \mathbf{r})$ is computed over a discrete mesh covering the focus area. In the resulting map, peaks are interpreted as areas with a high probability of finding a source. See Fig. 17 and Fig. 18. As also discussed in "Appendix: The Cross-spectral Imaging Function" on page 43, this interpretation is justified by the fact that in the far-field limit $I^2(\omega, \mathbf{r})$ is identical to the mean square value of the delay-and-sum expression, eq. (7). Due to this connection with the plane wave case, we can expect improved sidelobe levels from the self-term-free version of the imaging function, eq. (35):

$$J^2(\omega, \mathbf{r}) \equiv \frac{1}{\sqrt{M(M-1)}} \frac{\left| \sum_{m \neq n}^{M} C_{nm}(\omega) v_n(\mathbf{r}) v_m^*(\mathbf{r}) \right|}{\sqrt{\sum_{m \neq n}^{M} |v_n(\mathbf{r})|^2 |v_m(\mathbf{r})|^2}} \tag{36}$$

where the modified normalisation factor reflects the omission of the diagonal terms in the cross-spectral matrix. This modified normalisation factor ensures that the imaging functions I and J will be identical when focusing on a far-field point source on the array axis. The benefit of autospectra exclusion in the cross-spectral imaging function is illustrated in Fig. 10.

Array Design

The performance of a beamformer array is to a very large extent determined by the array geometry because this defines the beamformer response through the array pattern, cf. eq. (5). From the array pattern we can extract the maximum sidelobe level profile, which defines the ability to suppress ghost images as a function of frequency. This enables us to investigate the properties of a given array design. The reverse problem: how to design an array with a desired usable frequency range and resolution is more complicated. In this section we will review a number

Fig. 10. *Comparison of the output of three different beamforming algorithms for a configuration with two incoherent 3 kHz monopole sources of equal strength. The data were generated using the array shown in Fig. 4. In the legend I refers to the full cross-spectral imaging function, eq. (35), J is the cross-spectral imaging function, eq. (36), which excludes the autospectra, and B is the delay-and-sum algorithm, eq. (29). All curves are normalised to 0 dB at maximum*
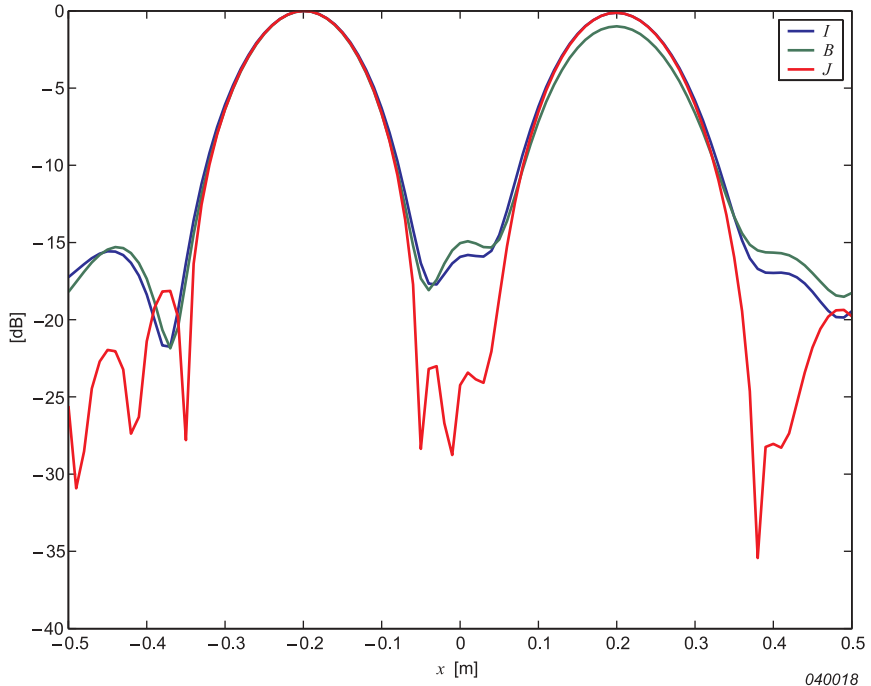
of array designs including both previously published, regular and irregular array designs and novel, numerically optimised array geometries, Fig. 11.

As we shall see below, the maximum sidelobe levels can be improved by shading, i.e., application of a smooth spatial window function. This improvement is, however, obtained at the expense of decreased resolution ability.

Regular Arrays

The simplest example of a regular array is the *uniform line array* (ULA), which is a one-dimensional linear array with equidistant microphone spacing. Though we are mainly interested in planar arrays, this array is well suited to demonstrate a number of important features of regular beamformer arrays. The microphone coor-

19

Fig. 11. Examples of regular and irregular array configurations. (a) 65-ch. cross-array, (b) 64-ch. grid array, (c) 66-ch. optimised random array, (d) 66-ch. Archimedean spiral array, (e) 66-ch. optimised wheel array, (f) 66-ch. optimised half-wheel array
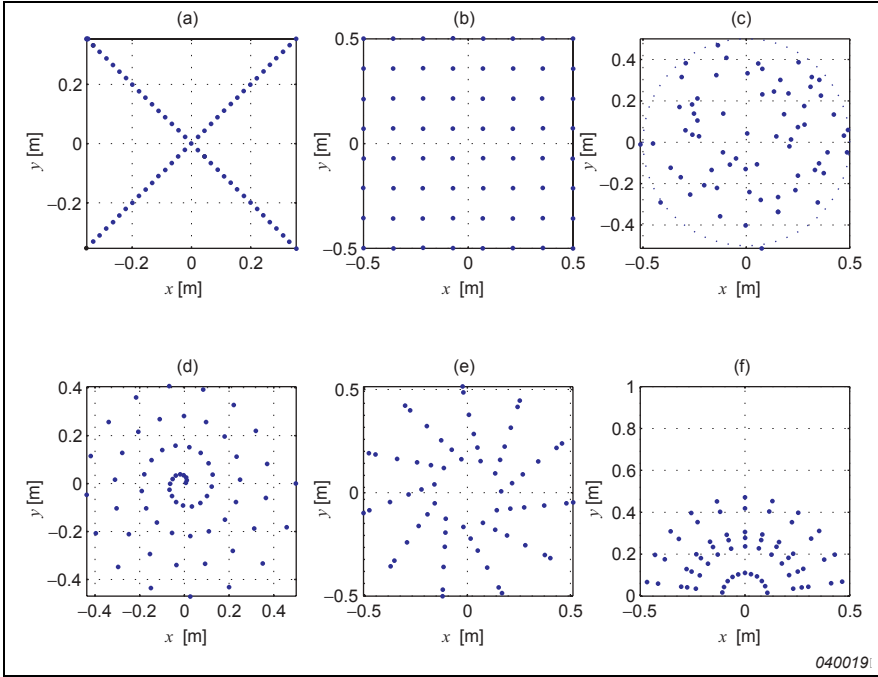
040019

dinates, x_m, of a ULA with microphone spacing d and $M \equiv 2M_{1/2}+1$ microphones can be written as:

$$x_m = (m - M_{1/2})d, \quad m = 0, \ldots, M - 1 \tag{37}$$

In the case of uniform shading, the corresponding array pattern [3] can be evaluated to:

$$W(K) = \frac{\sin(MKd/2)}{\sin(Kd/2)} \tag{38}$$

We notice that eq. (38) is a periodic function of K, the period equalling $2\pi/d$. In addition to the main lobe at $K = 0$, the ULA array pattern exhibits repetitions of the main lobe, so-called *grating lobes*, at the positions $K = p(2\pi/d)$, $p = \pm1, \pm2, \ldots$, Fig. 12(a).

20

Fig. 12. Graph (a) illustrates the side-lobe structure of a regular array with grid spacing d. In addition to the main lobe at $K = 0$, grating lobes occur at $K_x = \pm 2pK_N$, $K_N = \pi/d$, where p is a positive integer. Also shown is the wave number vector $\mathbf{k}_0$ at incidence angle 30°, and the focus direction wave number vector $\mathbf{k}$ in the direction $-30°$. In any case $|\mathbf{k}| = |\mathbf{k}_0| = k$ and we choose a frequency such that $k = 2K_N$. The projection k_x^0 of $\mathbf{k}_0$ onto the x-axis equals the Nyquist wave number K_N, and for this reason both the main lobe and the grating lobe at $2K_N$ contributes when beamforming is performed in the entire visible region (indicated by the green line) $-K_N < k_x < 3K_N$, where k_x is the projection of $\mathbf{k}$ on to the x-axis. In the resulting directional source map (b) a ghost source is seen at $\theta = -30°$ in addition to the true source at $\theta = 30°$. The directional source map (c) illustrates the situation for on-axis incidence at the same frequency

21
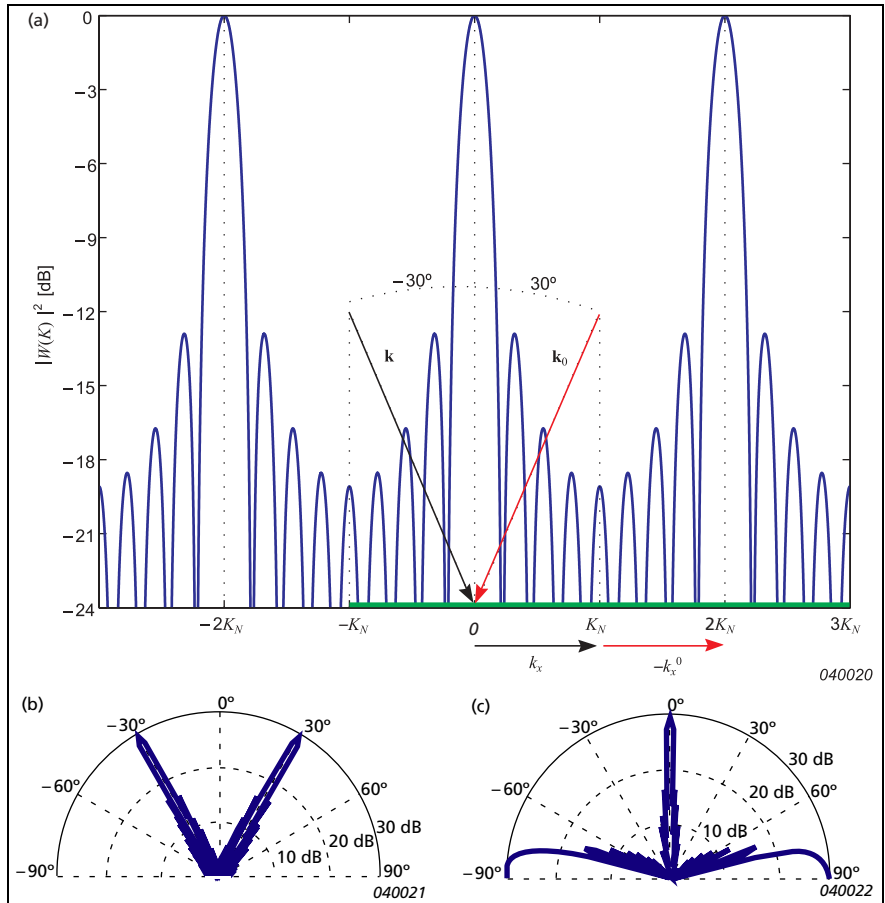
Plots of the ULA array pattern are depicted in Fig. 13 for both uniform shading and shading with a Hamming window. Comparing the two curves we see that the effect of the windowing is to lower the sidelobe levels and broaden the main lobe, that is, the dynamic range of the beamformer is improved at the cost of resolution.

Fig. 13. Plot of the array pattern for a uniform linear array with uniform shading and with a Hamming window applied. The effect of the window is to lower the sidelobes at the expense of widening the main lobe

040023
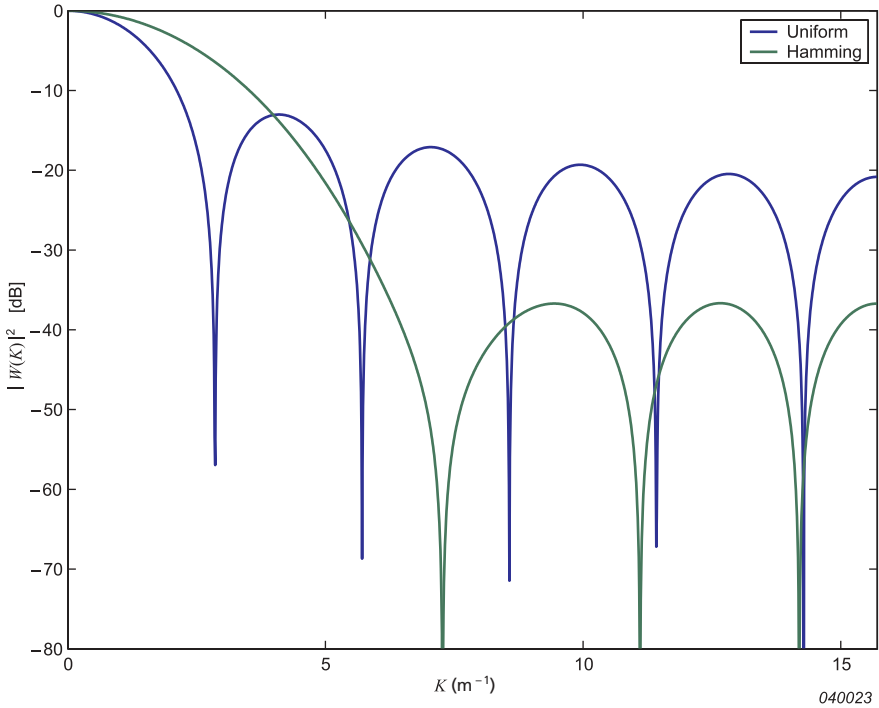
Spatial Aliasing

When sampling a time domain signal with a constant sampling rate $f_s = 1/T_s$, the highest frequency that can be unambiguously reconstructed is given by the Nyquist frequency, $f_N = f_s/2 = 1/(2T_s)$, or the corresponding angular frequency, $\omega_N = 2\pi f_N = \pi/T_s$ with a period of $T_N = 2T_s$ [4]. Similarly, when spatially sampling a signal with a sampling interval equal to d, then the spatial Nyquist angular frequency (the Nyquist wave number) is $K_N = \pi/d$ with a period length equal to $2d$. Plane waves with wavelength shorter than $\lambda_{min} = 2d$ therefore cannot be unambig-

uously reconstructed from the spatial samples, implying that the highest frequency f_{max} with sufficient sampling density is:

$$f_{max} = \frac{c}{\lambda_{min}} = \frac{c}{2d} \tag{39}$$

In general, time signals with frequencies $f \pm pf_s$, $p = 1, 2, \ldots$, cannot be distinguished when sampled with a sampling frequency $f_s = 2f_N$, and therefore they will all contribute when we estimate the content of, for example, the frequency f. Similarly, plane waves with angular frequencies $K \pm pK_s$, $p = 1, 2, \ldots$, on the measurement plane cannot be distinguished when sampled with a spatial angular sampling frequency $K_s = 2K_N$, and consequently they will all contribute when we estimate the content of any one of them in a spatially sampled sound field.

Typically, when aliasing occurs in the processing of a time domain signal, then there is a frequency component $f > f_N$ that is under-sampled and will contribute at a single frequency $f + pf_s$ in the "visible frequency range", $-f_N \le f + pf_s \le f_N$, p being an integer. The term "visible" means that only frequency components in that range will be estimated and used. Aliasing in beamforming happens in the same way, but here the "visible wave number range" is controlled by the beamforming algorithm and will not be restricted in the same way to $-K_N \le K + pK_s \le K_N$. As stated in eq. (19), the visible range will be up to $-2k \le K + pK_s \le 2k$, and therefore there may be several aliased components. The effect is that an angle θ of plane wave incidence will contribute at several aliased angles θ_a. This is illustrated in Fig. 12(a) where we consider measurement with a regular array with grid spacing d at a temporal frequency equal to twice the maximum frequency, eq. (39), for the array. The wave number vector $\mathbf{k}_0$ of a plane incident wave is therefore twice as long as the Nyquist wave number: $|\mathbf{k}_0| = k = 2K_N$, $K_N = \pi/d$. We consider a plane wave incident in the xz-plane at an angle $30°$ from the array axis, meaning that the projection of $\mathbf{k}_0$ on the array plane has length equal to the Nyquist wave number: $k_x^0 = -K_N$. According to eq. (5), the output from the beamformer will be given by $B(k_x, \omega) = P_0 W(k_x - k_x^0)$ when we focus on a plane wave incident with wave number vector $\mathbf{k}$ with x-component k_x. When focusing is scanned over all possible incident plane waves with wave number vectors $\mathbf{k}$ in the xz-plane, $|\mathbf{k}| = k$, then k_x will scan the interval from $-k = -2K_N$ to $k = 2K_N$, meaning that the argument $K_x = k_x - k_x^0$ to the array pattern will scan the interval from $-K_N = \pi/d$ to $3K_N = 3\pi/d$. By inspection of the array pattern in Fig. 12(a) we see that maximum output will be obtained both at the main lobe ($K_x = 0$) for $k_x = k_x^0 = -K_N$ and at the first grating lobe ($K_x = 2K_N$) for $k_x = -k_x^0 = K_N$. In the resulting directional source map, Fig. 12(b), the plane wave incident at $\theta = +30°$ contributes also as an aliasing component at $\theta_a = -30°$.

For on-axis incidence at the same frequency, the resulting directional source map is even more confusing since in addition to the main lobe, two grating lobes of the array pattern at $K_x = \pm 2K_N$ are included, Fig. 12(c).

The Grid Array

A straightforward realisation of a two-dimensional array is the grid array with microphone spacing d. Fig. 11(b) shows an example of an 8×8 grid array with microphone spacing $d = 1/7$ m, and hence the highest frequency is $f_{max} \approx 1.2$ kHz. The maximum sidelobe level for this grid array is depicted in Fig. 14 as a function of frequency. The sharp cut-off at the maximum frequency is a characteristic of regular arrays. When such an array is applied for beamforming at frequencies above f_{max}, the grating lobes may show up in the source map as false sources, so-called *ghost images*. The problem is illustrated in Fig. 17(c) for a single 5 kHz monopole and in Fig. 18(c) for a four-source configuration of 5 kHz monopoles. Clearly, the grating lobes introduce disturbing *ghost images* in the source map.

Fig. 14. Comparison of the Maximum Sidelobe Levels for the 1 m arrays depicted in Fig. 11. The Maximum Sidelobe Level function MSL(K), cf. eq. (18), is here shown as a function of frequency, f, which is related to the wave number K by f = Kc/4π, cf. eq. (19)
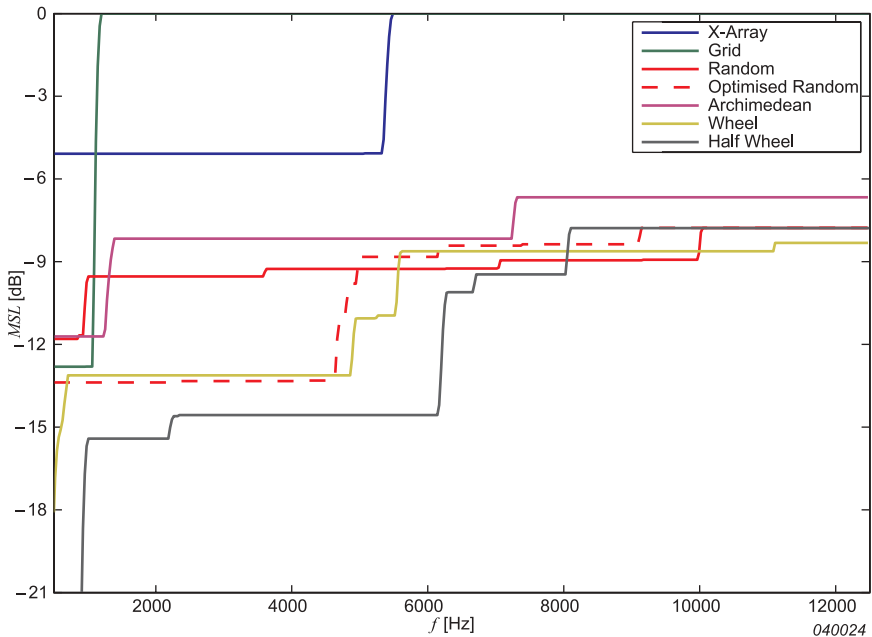
The Cross-array

The grid array can only be designed for higher frequencies by decreasing the grid spacing. For a fixed aperture size this is costly in terms of transducers and the resulting array may lose its acoustic transparency. With a given number of transducers and desired aperture size, an efficient way of constructing a regular array with large usable bandwidth is the cross-array, Fig. 11(a), which is a combination of two uniform linear arrays. If D is the aperture size and M is the number of transducers, the microphone spacing is approximately $D/(\sqrt{M} - 1)$ in the grid array and approximately $2D/(M - 1)$ in the cross-array. Thus the maximum frequency is a factor $(\sqrt{M} + 1)/2$ higher for the cross-array than for the grid array.

The cross-array array pattern exhibits high sidelobes along the directions defined by the constituting line arrays and good sidelobe suppression in all other directions, Fig. 17(a). In beamforming source reconstruction using the cross-array, the "ridges" protruding from the position of each source may interfere constructively and produce ghost images, Fig. 18(a).

Cross-array Beamforming Algorithm

The ghost-image problem caused by the structure of the array pattern can to some extent be circumvented by processing each line array separately and then combining the results [5]. Formally, the source mapping is obtained by taking the geometric mean $B_{\text{X-array}}(\mathbf{r}, \omega)$ of the beamformer outputs $B_1(\mathbf{r}, \omega)$, $B_2(\mathbf{r}, \omega)$ from the two Hanning weighted line arrays:

$$B_{\text{X-array}}(\mathbf{r}, \omega) = \sqrt{B_1(\mathbf{r}, \omega)B_2(\mathbf{r}, \omega)} \tag{40}$$

The result is a much improved sidelobe structure for single-source focusing, Fig. 17(b). Problems with ghost images for multi-source configurations cannot, however, be avoided, Fig. 18(b). Resolution is degraded compared to standard Delay-and-Sum or Cross-spectral beamforming because of the applied Hanning weighting.

Irregular Arrays

The major limitation of regular arrays is the previously described aliasing problem introduced by the repeated sampling spacing. This severe aliasing, producing ghost images of the same level as the true sources, can be avoided when the array geometry is totally non-redundant, that is, no difference vector between any two transducer positions is repeated. For non-redundant arrays, which typically have

an irregular or random geometry, the sidelobe structure does not exhibit the sharp cut-off frequency we have encountered for the regular arrays. Instead, the array patterns of irregular arrays have, in general, gradually increasing maximum sidelobe levels, Fig. 14.

In general, irregular (non-redundant) arrays outperform traditional regular array designs, but it is difficult to find out how the design should me made (or modified) to obtain high performance. Therefore, when designing irregular arrays for a given frequency range, one often resorts to a tedious trial and error cycle. The performance of parametric irregular arrays, for example, array geometries based on one or several concentric logarithmic spirals [6], or on an Archimedean spiral [7], Fig. 11(d), are easier to investigate because the range of a single or a few parameters can be tested systematically. In many cases, though, the *MSL* as a function of the relevant design parameter(s) exhibits highly erratic behaviour.

Another complication with irregular arrays is that, due to their complicated geometry, the transducer support structure can be difficult to realise. Both the support structure and the cabling are complicated and, as a consequence, operation in a practical measurement situation is difficult or tedious. Also, the need for high resolution at large measurement distances can only be met with relatively large dimensions of the arrays. Thus, an array with a diameter of several metres is often required. In connection with outdoor applications it is therefore of practical importance that the array construction allows for easy assembly and disassembly at the site of use, and for easy transport.

Optimised Arrays

An alternative approach to the problem of designing irregular arrays with a well-controlled performance is to use numerically optimised array geometries. Specifically, an array can be optimised to a given frequency range by adjusting the transducer coordinates so that the maximum sidelobes are minimised over the frequency range of the array's intended use:

$$\underset{\{\mathbf{r}_m\}}{\text{minimise}}\; MSL(K) \qquad \text{for} \qquad K < K_{\max} \tag{41}$$

where $K_{\max}$ is determined by the desired upper frequency and applied opening angle, cf. "Maximum Sidelobe Levels" on page 11. In the optimisation process the transducer coordinates are subject to certain geometrical constraints. Naturally, the transducer positions must not overlap, and we must also require that the positions

26

are confined within an area of linear dimension D, for example, a disc with diameter D or a box with side length D.

The simplest example of an optimised planar array geometry is the optimised random array. Fig. 11(c) shows the result of optimising the random array of Fig. 4 according to eq. (41) with a K_{max} corresponding to $f_{max} = 5\,\text{kHz}$, $K_{max} = K_{max}^{90°}(2\pi \cdot f_{max})$, cf. eq. (19). The geometry of the resulting array still looks random, but when comparing the sidelobe levels before and after optimisation, Fig. 14, it is noticed that the sidelobe levels are reduced by several dB for frequencies below f_{max}. The optimisation method thus provides an efficient and well-controlled method for decreasing the sidelobe levels over a given frequency range.

Brüel & Kjær Wheel Array

By optimising a random array, a beamformer with excellent performance can be achieved. From a practical point of view the random array is, however, difficult both to manufacture and operate, due to its complicated geometry. Also, the optimisation of a random array is numerically very demanding because of the large number of free variables.

Fig. 15 shows an example of a patented [8] Wheel Array design that is the result of an optimisation with the geometrical constraint that the transducers are confined to a set of tilted linear spokes. The patented design consists of typically an odd number N of identical line arrays arranged around a centre as spokes in a wheel, with identical angular spacing between the spokes. All spokes are tilted the same angle away from radial direction. The geometry is invariant under a rotation $n \cdot 360°/N$ around the centre, n being any integer.

Fig. 15. Wheel Array. All spokes are tilted the same angle away from radial direction, here illustrated by a lateral offset d
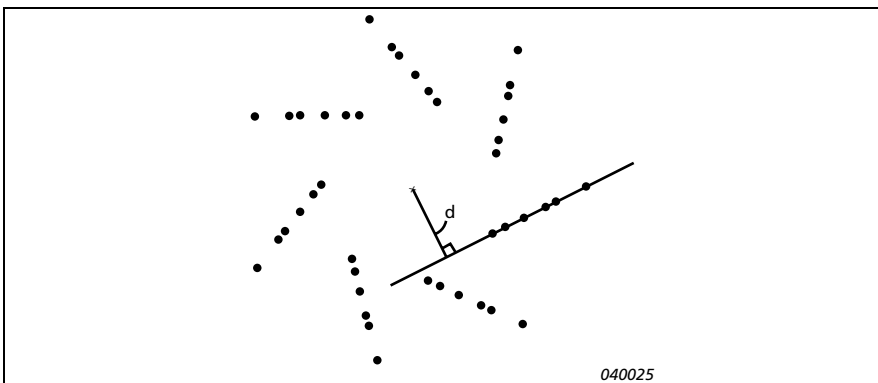

040025

Fig. 16. Example of 90-channel wheel array with integrated cabling

The mechanical design of the array shown in Fig. 16 is fully modular: all spokes can easily be detached from the supporting inner and outer rings which themselves can be disassembled. Thus the whole array structure can be disassembled and transported in a standard-sized flight case. Regarding the cabling, each spoke mounts 6 microphones, which through integrated cabling are connected to a common plug (LEMO-connector). Each spoke is then connected to a 6-channel (or 12-channel) input module through a single cable. Despite its irregularity the wheel array has its sensors grouped in easily identifiable logical units. In a practical meas-

urement situation, which requires channel detection, calibration and occasionally detection of hardware faults, this is a great advantage.

A variant of the wheel array is the half-wheel array, intended for measurements above a fully reflective ground/floor. In the half-wheel array, the spoke tilt angle is zero because the array design is required to be symmetric with respect to the ground floor, Fig. 11(f).

Comparison of the *MSL*-curves of a wheel array with other arrays with the same channel count and diameter shows that the wheel array performs better than the traditional regular arrays, Fig. 14. The optimised random array performs slightly better than the wheel array but, as mentioned above, this type of array is difficult to operate. Summarising, the wheel array combines high performance with easy operation and manufacturing.

Instrumentation

A complete PULSE-based beamforming system consists of the following main components:

- A beamforming array structure with transducers, cabling and optional Web camera.
- A PULSE front-end system
- PULSE data acquisition software including Data Recorder Type 7701 controlled by the Acoustic Test Consultant Type 7761
- A beamforming calculation module Type 7768
- For display of the results, Noise Source Identification Type 7752 is used

A complete configuration list is given in the Product Data for Type 7768.

Beamformer Arrays

There are several possibilities for beamformer array structures, including patented wheel arrays, traditional cross and grid arrays as well as other irregular array types (logarithmic spirals, Archimedean spirals). For optimal performance, we recommend one of our patented wheel types of array: see "Brüel & Kjær Wheel Array" on page 27.

The structures can be full arrays or "half arrays", where mirror-ground conditions can be utilised. A special possibility is flush-mounted microphones, which can be beneficial in wind-tunnel applications or at high frequencies to avoid diffraction in the microphones and in the support structure.

Fig. 17. Contour plots showing simulation results of source reconstruction using the arrays depicted in Fig. 11 applied with different beamforming algorithms. All data sets are normalised to 0 dB at maximum and the dynamic range is 15 dB. In the simulations, a 5 kHz monopole was placed in front of the array centre at 1 m distance. (a) and (b) show the results for the cross array, Fig. 11(a), using delay-and-sum and Hanning weighted cross-array beamforming, respectively ["Cross-array Beamforming Algorithm" on page 25]. (c) – (f) show the results of delay-and-sum beamforming for the grid array, the optimised random array, the Archimedean spiral array and the wheel array depicted in Fig. 11(b) – (e). (g) – (i) illustrate the outcome of applying cross-spectral beamforming with autospectra exclusion to the optimised random array, the Archimedean spiral array and the wheel array, respectively
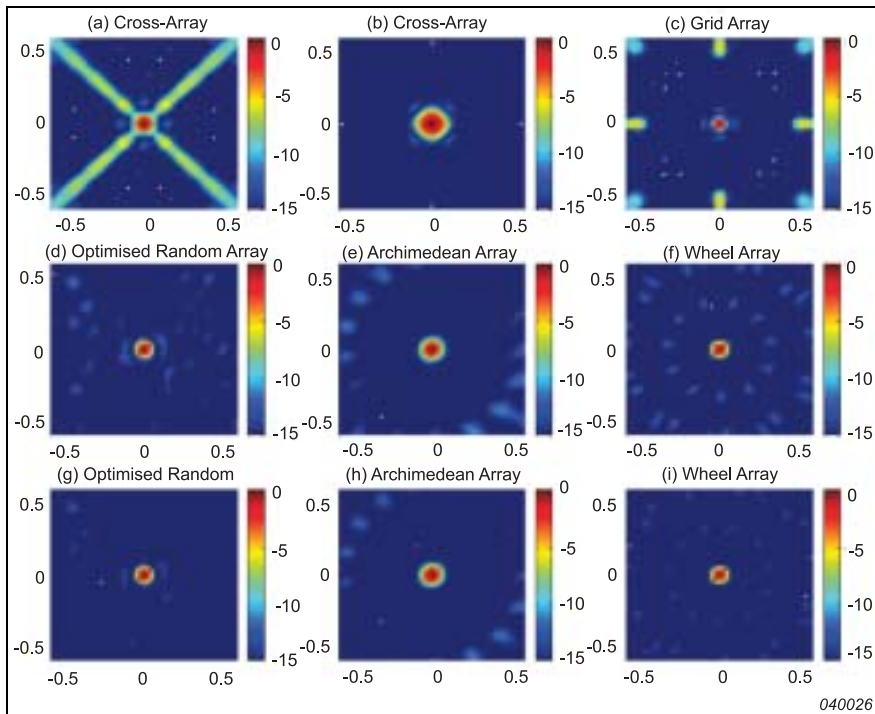
Transducers

Two types of array microphones are ideal for beamforming measurements. Array Microphone Type 4935 is ideal for measurement below 5 kHz, Type 4935-W001 extends the frequency range up to 10 kHz, and finally Array Microphone Type 4944 A is ideal for measurements up to 20 kHz and for array types with flush-mounted microphones. Both microphone types support IEEE 1451.4 Transducer

30

Fig. 18. Contour plots showing simulation results of source reconstruction using the arrays depicted in Fig. 11 applied with different beamforming algorithms. All data sets are normalised to 0 dB at maximum and the dynamic range is 15 dB. In the simulations, four 5 kHz monopoles were placed in front of the array at 1m distance. Green asterisks indicate the source positions. (a) and (b) show the results for the cross array, Fig. 11(a), using delay-and-sum and Hanning weighted cross-array beamforming, respectively ["Cross-array Beamforming Algorithm" on page 25]. (c) shows delay-and-sum beamforming with the grid array, and (d) – (f) give the results of using cross-spectral beamforming with the optimised random array, the Archimedean spiral array and the wheel array. The last row illustrates a mirror-ground situation. (g) represents delay-and-sum beamforming using the cross-array, while (h) and (i) show the corresponding results for the half-wheel array, Fig. 11(f), using mirror-ground delay-and-sum beamforming (h) and mirror-ground cross-spectral beamforming (i)
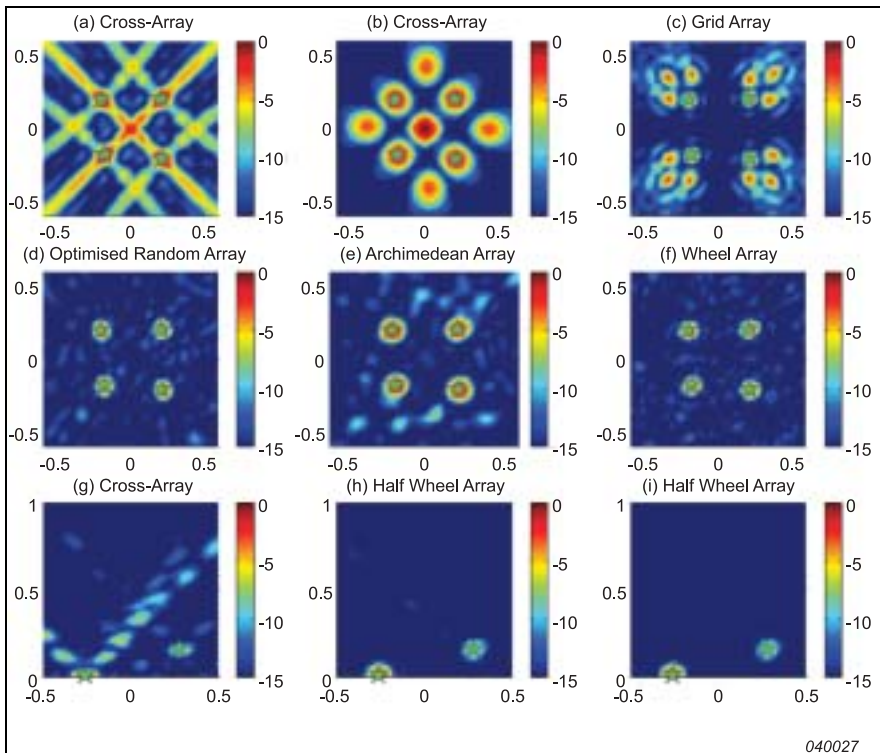
Electronic Data Sheet, which allows automatic transfer of the transducers' serial numbers and sensitivity data to be used directly in the application. Calibration can be performed on six microphones in parallel using the special pistonphone adaptor

WA 0728, and the system automatically detects which channels are being calibrated.

Other transducers such as hydrophones for underwater applications can also be used.

Data Acquisitions System and Beamforming Calculations

Data acquisition is performed using PULSE hardware and software. The measurement process is controlled by PULSE Acoustic Test Consultant (ATC) Type 7761 and involves use of PULSE Data Recorder Type 7701. ATC provides fast and easy setup of multichannel array systems, including automatic channel detection, parallel multichannel calibration, real-time level monitoring and on-line determination of channel status. The measured time data is stored in a PULSE database (based on Microsoft® SQL Server™), from which it can be retrieved for beamforming calculations using Type 7768.

When searching in large databases, measurements can be identified according to user-defined criteria based on meta-data stored with the measurement data.

From each measurement it is possible to perform multiple calculations, for example, by focusing on specific parts of the test object or on specific frequency bands. Also, it is possible to choose whether the calculation is performed with the free-field or mirror-ground algorithm (see Fig. 22 for a screen dump of the Calculation Setup dialog). Three different types of calculations are available: Stationary, Quasi-stationary and Non-stationary. The first two methods are based on the cross-spectral imaging function described in "Cross-spectral Imaging Function" on page 16. When "Stationary" is selected, the cross-spectra are averaged over the entire selected time interval before being applied in the cross-spectral imaging function with autospectrum exclusion, eq. (36). When "Quasi-stationary" is selected, the same procedure is performed in a number of subintervals where approximate stationarity can be assumed. This method is useful for the analysis of, for example, slow run-ups where the sound field can be assumed approximately stationary in narrow RPM intervals. With "Non-Stationary" selected, a time-domain beamforming calculation is performed in the following way: First an FFT is performed on the full selected time record length. Then the near-field Delay-and-Sum algorithm eq. (29) (normalised by the channel count) is applied for each FFT line. Finally, the frequency domain results are converted into time-domain using inverse FFT. The resulting time data can then be averaged in time intervals or, if a tachometer signal has been recorded, in angle-, tacho-, or RPM-intervals.

To display the result of a calculation using Noise Source Identification software Type 7752, simply drag and drop it into a display window. The display window contains both a map and a spectral view of the result.

These views are aligned, so the map always represents the frequency range selected by a delta-cursor in the spectrum, and the spectrum always shows the data for the selected cursor point on the map. Additionally, extensive display management tools are available, including zoom, scroll, tilt, rotate, and animation. Different calculations can be displayed in separate display windows for comparison, or in the same display for a complete 3D result.
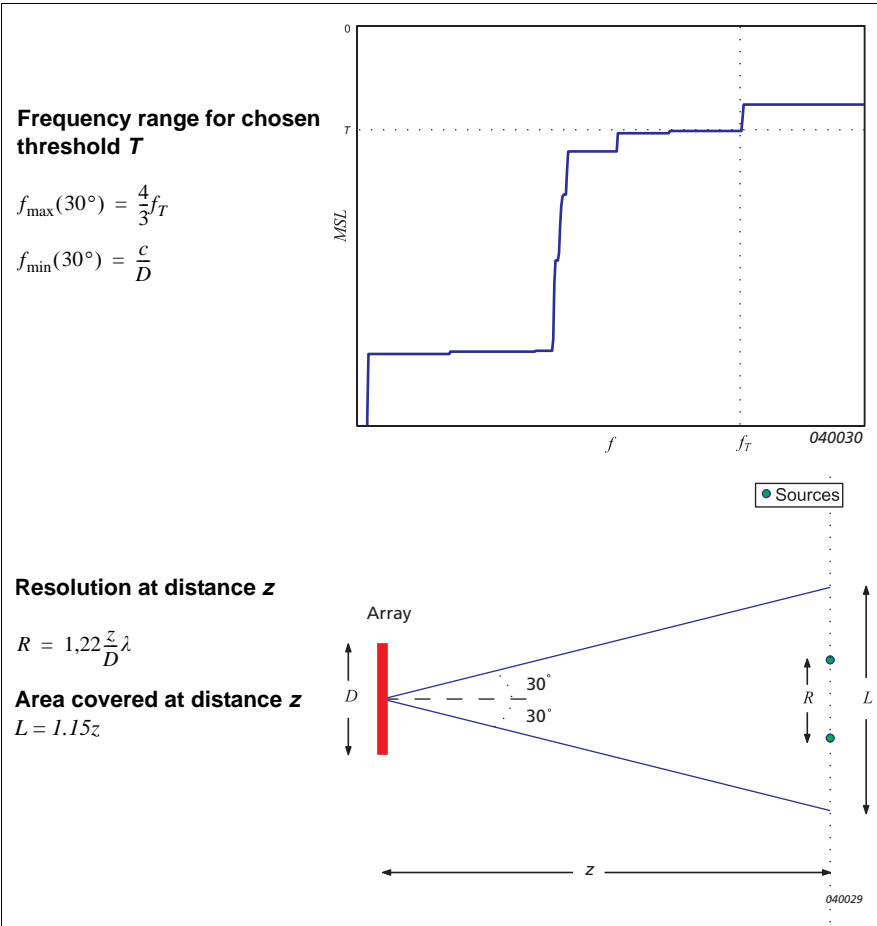
Practical Aspects of Designing and Using Beamformer Arrays

When designing an array for beamforming and when performing practical measurements, a number of practical aspects must be taken into account. These include the lower and upper frequency limitations of the array design, the *MSL* of the array defining its dynamic range, the array diameter, the measurement distance, the spatial resolution and the size of the mapping area. As will be explained below, these quantities are highly interconnected. The relations are summarised and illustrated in Table 1.

The Maximum Sidelobe Level (*MSL*) defines the dynamic range in the ability of the array to separate sources in different directions (see "Maximum Sidelobe Levels" on page 11). If, for example, the *MSL* is equal to –12 dB for frequencies up to 5 kHz and focusing within an angle of 30° from the axis, then within these limitations ghost images of a source in a single direction will always be suppressed by at least 12 dB relative to the strength of the real source. Other sources, which are not 12 dB weaker than the first source, will therefore not be hidden by the ghost images of the first source. The *MSL* is an important parameter when choosing an array design. Conversely, when interpreting results obtained by a given array, it is important to be aware of its *MSL*.

The acoustical environment, such as reflections and disturbing sources, must be considered when choosing an appropriate array design. A fully reflective floor can be exploited beneficially by using an array designed for the mirror-ground situation, for example, a half wheel, Fig. 11(f), and by applying a mirror-ground algorithm to the recorded signals. Other reflections will significantly disturb the measurement if the reflected contributions are within the dynamic range of the array, that is, if they are dampened relative to the direct contribution by less than the array's *MSL*. Strong disturbing sources or reflections *behind* a planar array should be avoided, as the array cannot distinguish a source behind the array from

Table 1. Beamformer properties at 30⁰ opening angle

Frequency range for chosen threshold *T* $$f_{\max}(30°) = \frac{4}{3}f_T$$ $$f_{\min}(30°) = \frac{c}{D}$$	
Resolution at distance *z* $$R = 1{,}22\frac{z}{D}\lambda$$ **Area covered at distance *z*** $$L = 1.15z$$	

its mirror image in the array plane. Sources behind the array will show up in the source map as image sources located *in front* of the array.

For many array designs there is no strict upper limit on the usable frequency range, because the *MSL* is slowly increasing with frequency for a given applied opening angle. In the case of regular arrays, however, the presence of grating lobes imposes a rather strict upper frequency limit. We can illustrate this by considering the *MSL* of the grid array, Fig. 14, with grid spacing *d*. This *MSL*-curve shows a

sharp cut-off at the spatial angular sampling frequency $K_s = 2K_N = 2\pi/d$, which for a 90° maximum off-axis focusing angle corresponds to a maximum frequency equal to $f_{max}(90°) = K_{max}c/4\pi$, see eq. (20). According to eq. (21), the maximum frequency for 30° off-axis angle is then given by $f_{max}(30°) = (4/3)f_{max}(90°)$. For the array in question, with grid spacing $d = 1/7$ m, this means that when applied with its maximum 90° opening angle, we must restrict ourselves to frequencies below $f_{max}(90°) = 1.2$ kHz, whereas the same array can be used up to $f_{max}(30°) = 1.6$ kHz if the maximum off-axis angle is reduced to 30°. The *MSL*-curve for irregular arrays does not have a sharp cut-off at a well-defined frequency. Instead the *MSL* deteriorates gradually with increasing frequency, Fig. 14. In this case, choosing a threshold level T can identify the upper usable frequency f_T (Table 1). The threshold level, T, should be chosen as the acceptable overall *MSL*, and in practical measurement situations a threshold level of $T = -10$ dB or lower should be preferred. The threshold frequency f_T is then the upper usable frequency at 90° off-axis angle, and at 30° maximum off-axis angle we have:

$$f_{max}(30°) = (4/3)f_T \tag{42}$$

The lower usable frequency of a beamformer array cannot be inferred from the arrays *MSL*-curve. Instead, considerations about the obtainable resolution at finite distance can give a useful number. A beamformer array relies on the phase differences between the signals recorded by its transducers to determine the angle of incidence of an incoming sound field. For wavelengths larger than the array aperture the phase differences become too small for the beamformer to effectively identify the angle of incidence, and as a consequence the ability to resolve different sources will be poor. We can determine a minimum frequency, f_{min}, by the requirement that when applying the beamformer array with a 30° maximum off-axis angle it must be possible to resolve two maximally separated monopoles with frequency f_{min}. Here, maximum separation means that the distance between the two sources is $2\tan(30°)z \approx 1.15z$ which is the linear size of the focus area at distance z for an opening angle of 30° around the axis. Then, referring to eq. (15) with $a = 1.22$, the lower frequency for an array with diameter D is determined from $1.15z = 1.22(z/D)[c/f_{min}(30°)]$, or

$$f_{min}(30°) \approx c/D \tag{43}$$

In many cases, however, the resolution will be too poor at frequencies as low as given by eq. (43).

Application Examples

The application examples given in here represent noise source location problems, where beamforming is an attractive measurement method.

A Vehicle in a Test Hall

The first example is measurement of the noise radiation from a complete vehicle. At high frequencies a complete vehicle will be much larger than the wavelength, meaning that Near-field Acoustical Holography (NAH) will require a huge number of measurement points. For the cases when the vehicle is operated in a steady state on a dynamometer drum in a test hall, a scanning technique – such as STSF – could be used to measure all these positions with a realistic microphone array. The measurement time will, however, be significant, and there will be problems such as stationarity and reference selection. For the case of run-up operating conditions (simulated pass-by), a scanning technique is not easy to use: RPM interval averaging will typically have to be used, and quasi-stationarity will have to be assumed in each interval, which is a problematic assumption. The main advantages of NAH (STSF) are:

- High resolution on the source plane – also at low frequencies
- Possibility to simulate source modifications on the source plane. For example, this enables contribution analysis in any far field position
- Source ranking based on calibrated intensity maps

Beamforming, on the other hand, provides the possibility of doing a broad-banded, one-shot measurement with an irregular array at some intermediate measurement distance, typically 3 –7 m. The directional contribution maps obtained from such a measurement will show the positions of the noise-radiating regions with the highest relative contributions to the noise at the array position. No calibrated source descriptor such as sound power can be achieved, however.

Since a Test Hall has a reflecting ground plane, it is obvious to measure with a half-wheel array.

A Vehicle in a Wind-tunnel

For measurements on a vehicle in a wind-tunnel, there are many similarities with measurements in a test hall: there is a reflecting ground plane allowing the use of a half-wheel array, and the source will be much larger than the wavelength at high frequencies. An additional condition is that measurements have to be taken at quite long distances to stay out of flow. This is natural for beamforming, but would further increase the size of the measurement area for NAH (STSF), and at

such large measurement distances NAH loses its ability to provide good low-frequency resolution. To maintain good low-frequency resolution with NAH, a more difficult in-flow scanning of a microphone array is required.

The 90-channel wheel array of Fig. 16 has been used to perform a measurement on a car in a wind tunnel. This array has a diameter of 2.4 m and provides low *MSL* (–14 dB) up to 3 kHz with 90° maximum off-axis angle and 4 kHz with 30° maximum off-axis angle. An alternative NAH measurement, also covering the frequency range up to 3 kHz, would require in-flow scanning of a microphone array over a grid covering the car side with a grid spacing not larger than 5 cm. The beamforming measurement is a simple "one-shot" recording taken with the 90-element array outside the flow region.

The vehicle was centred in the flow section, facing the wind, and the wind speed was set to 130 km/h. The wheel array was placed parallel to the side of the car at a distance of 3.3 m. The stationary beamforming calculation shown in Fig. 19 clearly

Fig. 19. Car in a wind-tunnel at 130 km/h wind speed

37
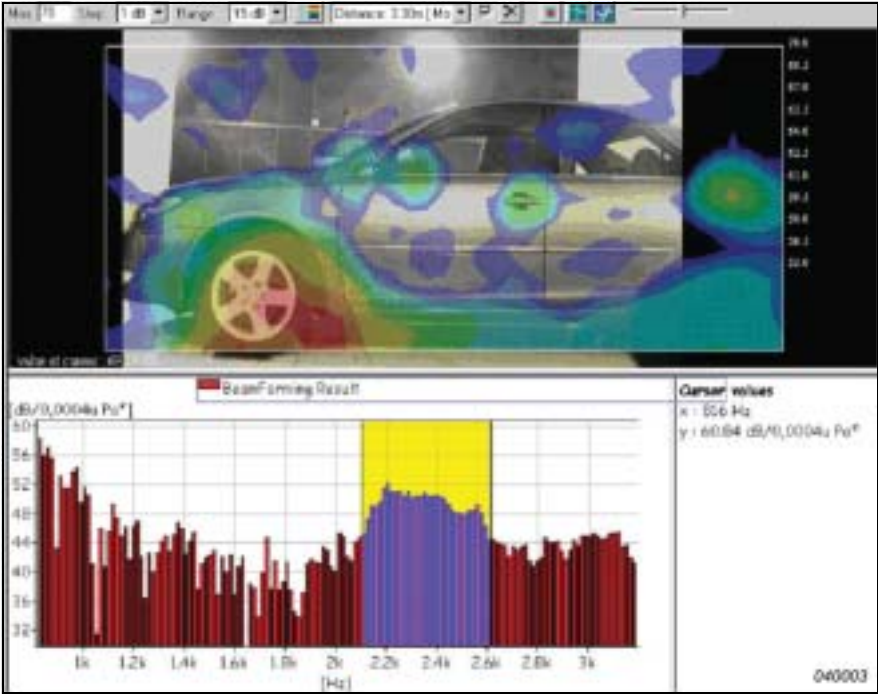
reveals noise radiation from the front wheel, the side mirror, the A-pillar and the door handle in the frequency interval from 2.1 kHz to 2.6 kHz. The spectrum plot represents the contour cursor position on the door handle, and the contour plot represents the frequency interval selected by the delta cursor in the spectrum plot. For this application, a low *MSL* (a large dynamic range) is very important to prevent ghost images from the strong radiation around the wheel to mask the other sources.

A Large Source (Crane)

Beamforming is a very powerful technique for noise source location on large sources up to rather high frequencies, requiring only a single recording with a microphone array. In this example, a 42-channel wheel array with a diameter of 1 m was positioned 7 m from a crane hoisting at maximum load, see Fig. 20. The array, the geometry of which is shown in Fig. 15, has *MSL* below –10.6 dB up to 4.8 kHz for 90° maximum off-axis angle and up to 6.4 kHz for 30° maximum off-

Fig. 20. Mobile crane hoisting at maximum load

38
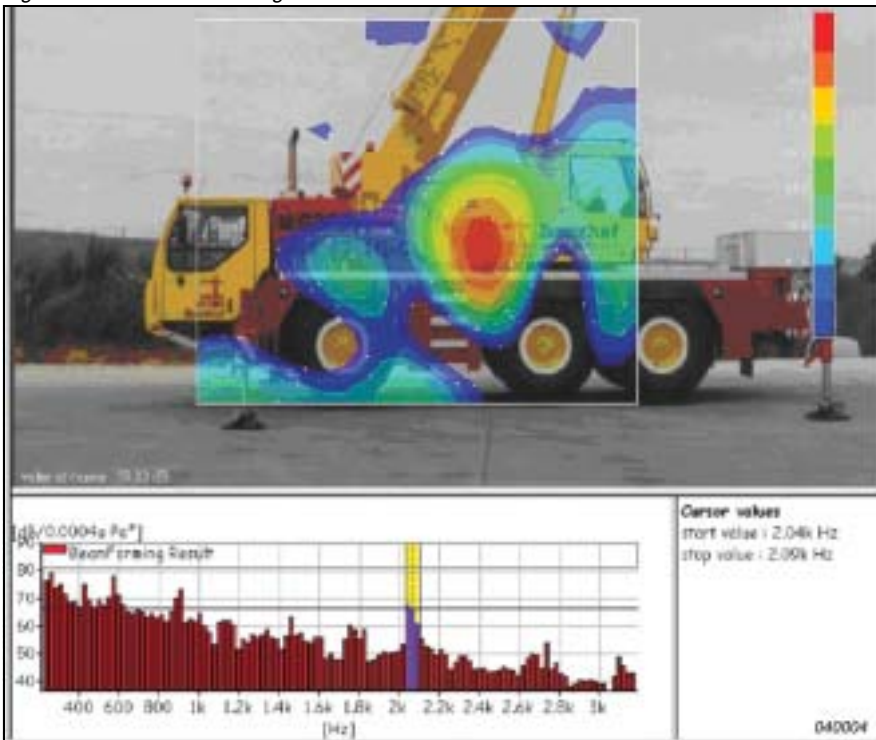
axis angle. The rather long measurement distance was chosen in order to get a large mapping area, at the sacrifice of resolution. According to the overview in Table 1, the size of the mapping area can be up to $1.15 \times 7\,\text{m} \approx 8\,\text{m}$ within the 30° maximum off-axis angle, but the resolution will be only $1.22 \times 7/1 \approx 8.5$ wavelengths.

Fig. 20 shows the source location for a frequency band around 2.05 kHz, where the spectrum shows a peak. The spectrum represents an area of high-level radiation over a cover plate that is probably resonating within the selected frequency band.

An Engine at High Frequencies

This example is a measurement on a car engine with a 66-element, 1 meter diameter wheel array. This wheel array has *MSL* below –10.4 dB up to 16 kHz with 90° maximum off-axis angle. The array was hanging approximately 0.9 m over an open engine compartment, with the engine running at 3500 RPM, and a single time history recording was made with a frequency bandwidth of 12.8 kHz. Fig. 21 contains the result of a Stationary beamforming calculation for the 6.3 kHz, 1/3-octave band, the contour interval being 1 dB.

*Fig. 21. Averaged 6.3 kHz, 1/3-octave band for a car engine*
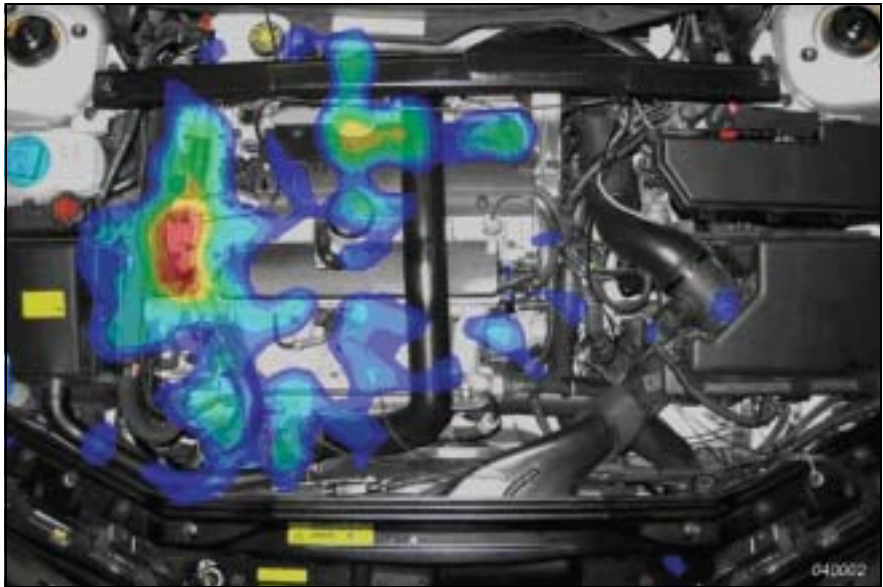
A NAH measurement covering the frequency range up to, for example, 8 kHz would require measurement over a regular rectangular grid of points with spacing around 2 cm. To cover the entire engine compartment would require approximately 2500 measurement positions, which should be compared with the 66 positions used by the beamformer. One major difference between the two techniques is that NAH can provide calibrated maps of Sound Intensity, Pressure and Particle Velocity close to the source, while with beamforming one can only get contour plots showing relative contributions to the sound field at the array position. No calibrated absolute levels near the source surface are obtained with beamforming.

Transient Analysis of Engine Noise Radiation

Another measurement was performed on the same engine at a constant speed of 2000 RPM using the same array at a distance of 81 cm from the nearest point on the engine. But now, in addition to the microphone signals, a tacho signal was also recorded to provide RPM and crank angle information, and a Non-stationary type of calculation was performed. Fig. 22 shows the Calculation Setup used to define the parameters in the calculation. Here, the time interval for processing, the size and resolution of the mapping area and the distance to the mapping area has been

Fig. 22. Calculation Setup
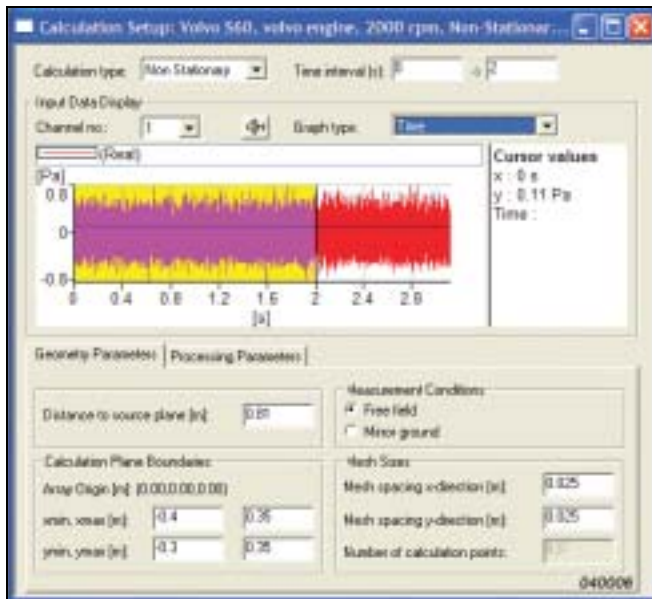
defined. Under the tab page named Processing Parameters, the frequency range and type of averaging have been chosen. In this case we have used 1/3-octave band filters and performed (crankshaft) Angle Interval averaging in intervals of 5°. Thus, for each 1/3-octave band we get 720/5 = 144 maps of the radiation during an engine cycle consisting of two revolutions. For each angle interval, averaging has been performed over all rotations within the selected time interval.

When doing angle interval averaging, one has to be aware of the time smearing performed by the impulse response of the frequency band-pass filters used. With a frequency bandwidth equal to B, the impulse response will have duration around $1/B$. This should be related to the time for one rotation, which is 60 s/RPM. An impulse will therefore be smeared over an angle of approximate width $6° \cdot RPM/B$. For the present measurement we shall be looking at data for the 3.15 kHz, 1/3-octave band, and the smearing angle turns out to be approximately 15°.

A typical result is shown in Fig. 23. The angle meter shows a crank angle interval from 615° to 620° and the spectrum plot shows that only the 3.15 kHz, 1/3-octave band has been selected for mapping. The spectrum represents the cursor position on the peak of the contour plot. Clearly, the 3.15 kHz, 1/3-octave band is very strong at the chosen peak position. To the left of the Angle (and RPM) meter, the variation with angle at the cursor position is plotted. The sharp peaks indicate that the radiation at the peak position is very impulsive and concentrated at a few discrete shaft angles.

Another typical type of analysis would be averaging in RPM intervals for run-up measurements.

For the present measurement, we used only a single tacho signal providing a single impulse per cycle (of two revolutions). This provides a unique identification of a reference angular position during each cycle, but it does not necessarily allow an accurate estimation of the angle during the entire cycle. For this, the system supports the use of a second high-resolution tacho signal.

Conclusions

Beamforming is a noise source location method based on measurements with a planar array of microphones or hydrophones at an intermediate distance from the source. The beamforming calculation can then basically resolve the relative contributions from different directions to the sound field seen by the array. Pure directional resolution would correspond to focus at infinite distance. Our implementations always focus on a source plane parallel with the array plane, i.e.,
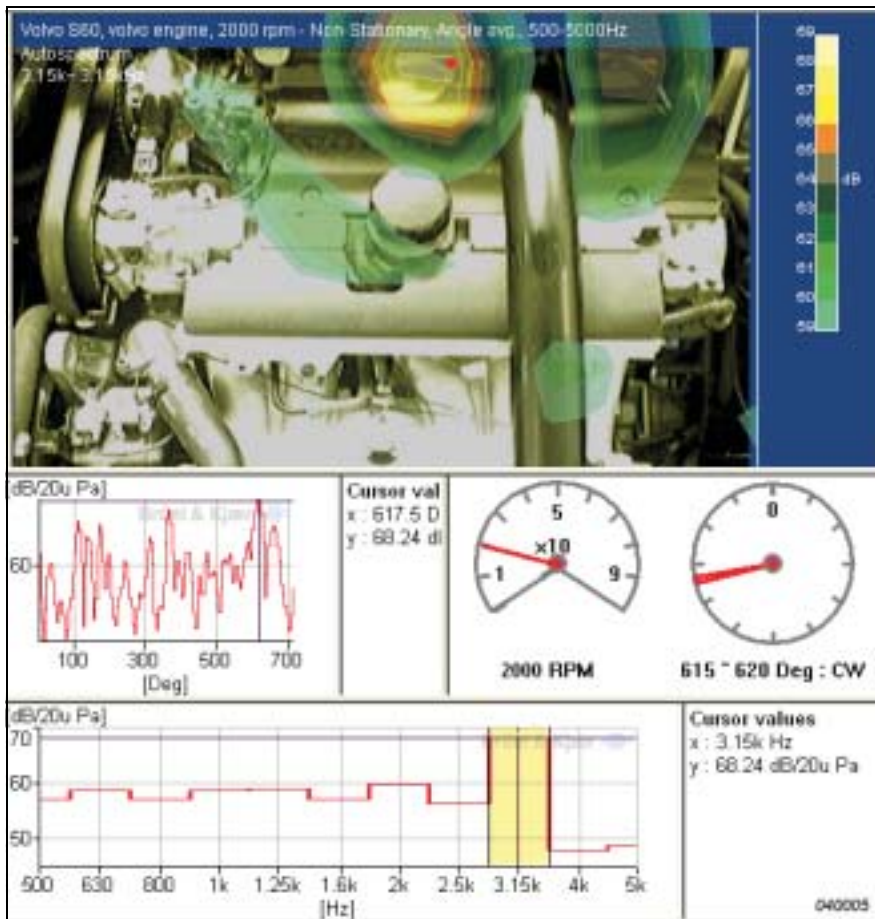
at finite distance, but still the method maps only relative contributions: no cali-
brated maps of sound field parameters near the source can be obtained. On the
other hand, a single measurement with an array of typically 42 – 90 transducers
can map a large source area up to high frequencies. The map can cover directions
up to approximately 30° from the array axis. Typically, a resolution of around one
wavelength can be obtained, which is almost as good as holography at high fre-

quencies, but at low frequencies holography can do much better. At very high frequencies, on the other hand, where holography is not feasible because of the required half-wavelength microphone grid spacing, beamforming can provide high resolution with relatively few measurement points.

The basic principle of beamforming has been outlined, and the performance of different array designs has been analysed and compared. The wheel array design, which is patented by Brüel & Kjær, has been shown to offer some distinct advantages: a combination of high performance and ease of handling. A new, self-term-free, cross-spectral beamforming algorithm has been described and shown to offer: (i) suppression of noise in the individual measurement channels, (ii) suppression of sidelobes (and thus of ghost images) and (iii) a natural distance correction for the individual array transducers when the array is used at a finite distance. The measurement system has been described together with guidelines for design and use of the system, and finally some typical application examples have been presented.

Appendix: The Cross-spectral Imaging Function

In this appendix we derive the Cross-spectral Imaging function applied in PULSE Stationary Beamforming. For each position on the source plane, the estimated source strength reflects how well the sound field from a monopole point source at that position fits the sound field measured by the array. The approach is inspired by reference [9].

The error function defined in eq. (34):

$$E(a, \mathbf{r}) = \sum_{m,n=1}^{M} \left| C_{nm} - C_{nm}^{\text{mod}} \right|^2 = \sum_{m,n=1}^{M} \left| C_{nm} - a v_n^*(\mathbf{r}) v_m(\mathbf{r}) \right|^2 \qquad (A.1)$$

can be written in a form that is convenient for the derivations, if we stack all the columns of the cross-spectral matrix $[C_{nm}]$ in a single-column matrix, and arrange the elements $[v_n^* v_m]$ in a similar matrix:

$$\mathbf{g} = [C_{nm}]$$

$$\mathbf{h}(\mathbf{r}) = \left[v_n^*(\mathbf{r}) v_m(\mathbf{r}) \right] \qquad (A.2)$$

For each position $\mathbf{r}$, we first determine the monopole strength $\hat{a}$ that minimises the error function, eq. (A.1). To do this we notice that the error function is mini-

mised by least squares solution of $\mathbf{g} \approx a\mathbf{h}$, which upon multiplication from the left with $\mathbf{h}^{\dagger}$ leads to:

$$\hat{a}(\mathbf{r}) = \mathbf{h}^{\dagger}\mathbf{g}/\mathbf{h}^{\dagger}\mathbf{h} \qquad \text{(\dagger\ transposed complex conjugate)} \qquad (A.3)$$

Appealing to the fact that the cross-spectral matrix is Hermitian and to the definition (A.2) of $\mathbf{h}$ and $\mathbf{g}$, we see that $\mathbf{h}^{\dagger}\mathbf{g}$ is real and equal to $\mathbf{g}^{\dagger}\mathbf{h}$. Therefore $\hat{a}$ is also real.

Use of eq. (A.2), eq. (A.3) and the relation $\mathbf{g}^{\dagger}\mathbf{h} = \mathbf{h}^{\dagger}\mathbf{g}$ in eq. (A.1) leads to the following expression for the error function:

$$E(\hat{a}, \mathbf{r}) = \left| \mathbf{g} - \hat{a}\mathbf{h}(\mathbf{r}) \right|^2 = \mathbf{g}^{\dagger}\mathbf{g} - \hat{a}(\mathbf{h}^{\dagger}\mathbf{g} + \mathbf{g}^{\dagger}\mathbf{h}) + \hat{a}^2 \mathbf{h}^{\dagger}\mathbf{h} = \mathbf{g}^{\dagger}\mathbf{g} - \frac{(\mathbf{h}^{\dagger}\mathbf{g})^2}{\mathbf{h}^{\dagger}\mathbf{h}} \quad (A.4)$$

Minimising the error function over all $\mathbf{r}$ thus corresponds to maximising the *Imaging Function*, $I(\omega, \mathbf{r})$,

$$I^4(\omega, \mathbf{r}) \equiv \frac{(\mathbf{h}^{\dagger}\mathbf{g})^2}{\mathbf{h}^{\dagger}\mathbf{h}} = \frac{\left| \displaystyle\sum_{m, n = 1}^{M} C_{nm}(\omega) v_n(\mathbf{r}) v_m^{*}(\mathbf{r}) \right|^2}{\displaystyle\sum_{m, n = 1}^{M} \left| v_n^{*}(\mathbf{r}) v_m(\mathbf{r}) \right|^2} \qquad (A.5)$$

over all $\mathbf{r}$ (we choose the definition I^4 since eq. (A.5) has units of power squared). In practice $I(\omega, \mathbf{r})$ is computed over a discrete mesh covering the focus area. In the resulting map, peaks are interpreted as areas with a high probability of finding a source. This interpretation can be justified if we compare the imaging function in the far field with the corresponding expression for the Delay-and-Sum beamformer, eq. (7). For large $R \equiv |\mathbf{r}|$ the approximation $|\mathbf{r}_m - \mathbf{r}| \equiv R_m \approx R$ is valid in connection with the amplitude of $v_m(\mathbf{r}) \equiv v(\mathbf{r}_m - \mathbf{r})$. In the far-field limit eq. (A.5) can therefore be approximated by:

$$I^4 = \frac{R^4 \left| \sum\limits_{m,\,n=1}^{M} C_{nm} v_n v_m^* \right|^2}{R^4 \sum\limits_{m,\,n=1}^{M} \left| v_n^* v_m \right|^2} \approx \frac{\left| \sum\limits_{m,\,n=1}^{M} C_{nm} e^{-jkR_n} e^{jkR_m} \right|^2}{\sum\limits_{m,\,n=1}^{M} \left| e^{-jkR_n} e^{jkR_m} \right|^2}$$

$$= \frac{1}{M^2} \left| \sum\limits_{m,\,n=1}^{M} C_{nm} e^{-jk(R_n - R_m)} \right|^2 \tag{A.6}$$

Expanding the square of eq. (7) and taking the average we find:

$$\overline{|B|^2} = \frac{1}{M^2} \sum\limits_{m,\,n=1}^{M} \overline{P_n^* P_m}\, e^{-jk\boldsymbol{\kappa}(\mathbf{r}_m - \mathbf{r}_n)} = \frac{1}{M^2} \sum\limits_{m,\,n=1}^{M} C_{nm} e^{-jk(R_n - R_m)} \tag{A.7}$$

where we have used that the difference in travel paths $R_n - R_m$ equals the projection difference $\boldsymbol{\kappa} \cdot (\mathbf{r}_m - \mathbf{r}_n)$, Fig. A1. Obviously, we have:

$$I^2/M = \overline{|B|^2}$$

which shows us that the imaging function in the far field, when normalised by the channel count, equals the output of the Delay-and-Sum beamformer. This observation justifies the chosen interpretation. The normalisation factor has been included in eq. (35).

Fig. A1. For a source in the far field, the difference, $R_n - R_m$, in the propagation path length to the transducers at $\mathbf{r}_n$ and $\mathbf{r}_m$ can be calculated from the diagram
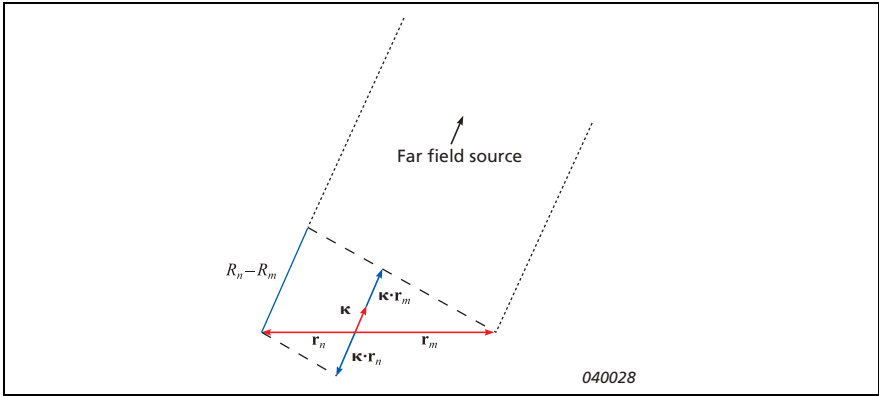
It could seem obvious to map the monopole strength $\hat{a}(\mathbf{r})$ of eq. (A.3) instead of the imaging function $I^2(\mathbf{r})$ that represents the reduction of the cross-spectral modelling error across the array. The main problem with $\hat{a}(\mathbf{r})$ is that the amplitude will increase when the distance to the array is increasing. So at angles far away from the array axis, $\hat{a}(\mathbf{r})$ will tend to predict unrealistically high levels.

The summations in eq. (A.5) can be rewritten in matrix form as:

$$\sum_{m,\,n\,=\,1}^{M} C_{nm} v_n v_m^* = \mathbf{v}^T \mathbf{C} \mathbf{v}^*$$

$$\sum_{m,\,n\,=\,1}^{M} |v_n|^2 |v_m^*|^2 = \mathbf{w}^T \mathbf{1} \mathbf{w}^*$$

(A.8)

where $\mathbf{v}$ and $\mathbf{w}$ are the column vectors $\mathbf{v} = [v_m]$ and $\mathbf{w} = [|v_m|^2]$, and where $\mathbf{1}$ is an M by M unity matrix with all elements equal to 1. The exclusion of autospectra can be formulated by introducing modified versions $\mathbf{C}'$ and $\mathbf{1}'$ of the cross-spectral matrix and the unity matrix, respectively, where zeros have replaced all diagonal elements. Then the imaging function, eq. (36), can be expressed as:

$$J^2(\omega, \mathbf{r}) = \frac{1}{\sqrt{M(M-1)}} \frac{\left| \mathbf{v}^T \mathbf{C}' \mathbf{v}^* \right|}{\sqrt{\mathbf{w}^T \mathbf{1}' \mathbf{w}^*}}$$

(A.9)

Mirror-Ground Implementation

In the case of a fully reflective surface perpendicular to the array plane, we can alter eq. (A.9) to make use of the fact that beyond the real sources there will seem to be equally strong image sources. The presence of a "mirror ground" is equivalent to a free-field situation, where we have no mirror ground, but instead image sources in addition to the real sources. The resulting sound field will be image symmetric in the (original) ground plane, so therefore we can assume a mirror array that will measure exactly the same as the real array. If we let $\hat{v}_m(\mathbf{r})$ be the steering vector component from the mth transducer in the mirror array to the source at position $\mathbf{r}$ we can obtain a mirror-ground version of eq. (A.9) by using the expanded column vectors $\tilde{\mathbf{v}}$, $\tilde{\mathbf{w}}$ and the expanded cross-spectral matrix $\tilde{C}$ defined by:

$$\tilde{\mathbf{v}} = \begin{bmatrix} \mathbf{v} \\ \hat{\mathbf{v}} \end{bmatrix}, \qquad \tilde{\mathbf{w}} = \begin{bmatrix} \mathbf{w} \\ \hat{\mathbf{w}} \end{bmatrix}, \qquad \tilde{\mathbf{C}} = \begin{bmatrix} \mathbf{C}' & \mathbf{C}' \\ \mathbf{C}' & \mathbf{C}' \end{bmatrix}$$

(A.10)

The cross-spectral imaging function for the mirror-ground situation is then:

$$\tilde{J}^2(\omega, \mathbf{r}) = \frac{1}{\sqrt{2M(2M-2)}} \frac{\left|\tilde{\mathbf{v}}^T \tilde{\mathbf{C}} \tilde{\mathbf{v}}^*\right|}{\sqrt{\tilde{\mathbf{w}}^T \tilde{\mathbf{1}} \tilde{\mathbf{w}}^*}} \tag{A.11}$$

The normalising factor is here $2M(2M-2)$, since now $4M$ elements out of $4M^2$ in $\tilde{\mathbf{C}}$ equal zero, and $\tilde{\mathbf{1}}$ is constructed from $\mathbf{1}'$ exactly as $\tilde{\mathbf{C}}$ is constructed from $\mathbf{C}'$.

Appendix: Resolution

With reference to Fig. 5, we can evaluate the resolution as follows. As stated in "Resolution" on page 8, two incident plane waves of equal amplitude with wave number vectors $\mathbf{k}_1$ and $\mathbf{k}_2$, $|\mathbf{k}_1| = |\mathbf{k}_2| = k$, can be resolved only if the projections $\hat{\mathbf{k}}_1$ and $\hat{\mathbf{k}}_2$ of $\mathbf{k}_1$ and $\mathbf{k}_2$ on the array plane are not within $R_K = K^0_{min}$ from each other. Here, R_K is the main-lobe width in the array pattern $W(\mathbf{K})$, and K^0_{min} is the position of the first minimum of the array pattern. In Fig. 5 we have

$$\left|\hat{\mathbf{k}}_2 - \hat{\mathbf{k}}_1\right| = R_K$$

so the two plane waves are just exactly resolvable.

In the focus plane, we shall look only at the resolution in the radial direction, that is, in the direction away from the array axis. We choose to look at the resolution along the x-axis. The plane wave with wave number vector $\mathbf{k}_1$ is incident at an angle θ from the array axis, and the exactly resolvable plane wave with wave number vector $\mathbf{k}_2$ is incident at an angle $\theta + R_\theta$ from the axis, R_θ being the angular resolution in the radial direction. These two directions span the resolution R along the x-axis at the distance z from the array plane (on the focus plane).

In the derivation we will now assume a very fine resolution, meaning that we can consider the resolutions in K, θ and x to be differential: $R_K = dK$, $R_\theta = d\theta$ and $R = dx$. From $K = k\sin(\theta)$ we get $dK = k\cos\theta d\theta$ and therefore:

$$d\theta = \frac{dK}{k\cos\theta}$$

From the relation $x = z\,\mathrm{tg}(\theta)$ we get:

$$dx = \frac{z\,d\theta}{\cos^2\theta}$$

and combination of the two above relations leads to:

$$dx = \frac{z\,dK}{k}\frac{1}{\cos^3\theta}$$

Finally, we replace the differential resolutions with the real finite resolutions and get:

$$R \approx \frac{z\,R_K}{k}\frac{1}{\cos^3\theta}$$

References

[1]   Maynard J.D., Williams E.G. and Lee Y., "*Nearfield acoustical holography: I. Theory of generalized holography and the development of NAH*", J. Acoust. Soc. Am. 78(4), 1985, pp. 1395 – 1413.

[2]   Hald J., "*STSF – a unique technique for scan-based Near-field Acoustic Holography without restrictions on coherence*", Brüel & Kjær Technical Review No. 1, 1989, pp. 1 – 50.

[3]   Johnson D. H. and Dudgeon D. E., "*Array Signal Processing: Concepts and Techniques*", Prentice Hall, New Jersey, 1993.

[4]   Proakis J.G. and Manolakis D. G., "*Digital Signal Processing, Principles, Algorithms, and Applications*", 3rd Edition, Prentice Hall, New Jersey, 1996.

[5]   Yasushi Takano, "*Two-dimensional Microphone Array System for Measuring Distribution of Aerodynamic Noise-sources on High-speed Trains*", International Symposium on Simulation, Visualization and Auralization for Acoustic Research and Education, Tokyo, 1997

[6]   Underbrink J. R. and Dougherty R. P., "*Array Design for Non-intrusive Measurement of Noise Sources*", Proceedings of Noise-Con 96, pp. 757 – 762, 1996.

[7]   Nordborg A., Wedemann J. and Willenbrink L., "*Optimum Array Microphone Configuration*", Proceedings of Internoise 2000.

[8]   Danish patent No. PA 2002 00412.

[9]   Elias G., Proceedings of Internoise 1995, pp.1175 – 1178.

Previously issued numbers of
Brüel & Kjær Technical Review

Special technical literature

Brüel & Kjær publishes a variety of technical literature which can be obtained from your local Brüel & Kjær representative.

The following literature is presently available:

- Catalogues (several languages)
- Product Data Sheets (English, German, French,)

Furthermore, back copies of the Technical Review can be supplied as listed above. Older issues may be obtained provided they are still in stock.

Brüel & Kjær